

ABSTRACT

Title of thesis: PATTERNED NICKEL ANODE STABILITY
IN SOFC ENVIRONMENTS WITH H₂, CO
AND CH₄ FUEL FEEDS

Benjamin Paul Becker, Master of Science, 2005

Directed By: Professor Gregory S. Jackson, Department of
Mechanical Engineering

Single cell solid oxide fuel cells supported on single crystal YSZ electrolytes with patterned Ni anodes fabricated through sputter deposition and photolithographic techniques and with porous LSM/YSZ cermet cathodes were tested electrochemically to assess the stability of the Ni anodes in SOFC environments. Anode stability and electrochemical performance for H₂, CO and CH₄ electrochemical oxidation were characterized at cell temperatures between 750 °C and 800 °C under humidified ($P_{H_2O}/P_{fuel} = 0.05$) conditions. Changes in performance of anodes polarized by typical working fuel cell overpotentials (100 - 200 mV) were compared to anodes kept at open circuit conditions. An increase in surface roughness was much greater for the polarized anodes than those kept under open circuit conditions. Electrochemical impedance spectroscopy and sweep voltammetry, over 10 continuous hours of testing, consistently showed constant performance for the polarized anodes and a drop in performance for the open circuit anodes.

PATTERNED NICKEL ANODE STABILITY IN SOFC ENVIRONMENTS WITH
H₂, CO AND CH₄ FUEL FEEDS

By

Benjamin Paul Becker

Thesis submitted to the Faculty of the Graduate School of the
University of Maryland, College Park, in partial fulfillment
of the requirements for the degree of
**Master of Science in
Mechanical Engineering**
2005

Advisory Committee:

Assistant Professor Bao Yang, Chair
Associate Professor Gregory S. Jackson
Professor Michael R. Zachariah

© Copyright by
Benjamin Paul Becker
2005

Acknowledgements

I would like to thank my advisor *Prof. Gregory S. Jackson* for his support and guidance throughout the production of this thesis and my time as a graduate student. He dedicated time and effort, much more than expected to listen to my difficulties and help me learn and succeed. His flexibility, friendliness and encouragement made completing my work at the University of Maryland very pleasant and rewarding. I also would like to thank my colleagues at The Center for Fuel Cell Research *Dr. Mary Sukeshini* and *Bahman Habibzadeh* for their contributions to this work. *Dr. Sukeshini* was always willing to explain the physics associated with fuel cells and help interpret electrochemical data. *Bahman Habibzadeh* shared the work of constructing and running experiments and helped me through many of the difficulties of graduate studies.

Thanks go to my colleagues at the Biochemistry Department: *Oktay Demerican*, *Mike Pomfret*, *Prof. Bryan Eichhorn* and *Prof. Rob Walker*. *Oktay Demerican* provided the materials and procedure necessary for cathode fabrication and assisted in analysis of XRD data. *Mike Pomfret* operated the Raman spectrometer on post-experimental patterned anodes and helped interpret the results. And a special thanks to all my colleagues for being friendly co-workers who made the workplace enjoyable.

Other people who helped make this thesis possible include: Tom Loughran who deposited many Ni coatings and who shared his expertise in photolithographic

techniques, *John Barry*, *Nolan Ballew* and *Jon Hummel* for their help in sputtering Ni coatings and finally *Tim Maugel* for operating the SEM and EDAX instrument.

Thanks also to *Prof. Michael R. Zachariah* and *Prof. Bao Yang* for being a part of my defense committee.

And finally I would like to thank my family for their support throughout my time as a graduate student and for providing an environment of encouragement that gave me the ability to take on graduate level study.

Table of Contents

Acknowledgements.....	ii
Table of Contents	iv
List of Tables	v
List of Figures	vi
Chapter 1: General Introduction	1
1.1 Introduction to Fuel Cells	1
1.2 The Solid Oxide Fuel Cell	6
1.2.1 SOFC Materials	11
1.2.2 SOFC Performance	15
1.3 Patterned Anodes for Understanding η_{act} and SOFC Kinetics.....	20
1.4 Objectives of the Current Study.....	22
Chapter 2: Experimental	24
2.1 MEA Fabrication	24
2.1.1 Cathode Fabrication	25
2.1.2 Anode Microfabrication.....	26
2.2 Experimental Setup.....	35
2.2.1 MEA Wiring	35
2.2.2 Experimental Rig	40
2.2.3 Temperature and Flow Control.....	44
2.3 Electrochemical Measurements	45
2.4 Range of Conditions Studied	49
Chapter 3: Non-electrochemical Test Results.....	55
Chapter 4: H ₂ Oxidation.....	66
Chapter 5: CO Oxidation	77
Chapter 6: CH ₄ Oxidation.....	84
Chapter 7: Conclusions	92
Appendix A. Patterned Ni Anode Defects.....	95
Bibliography	98

List of Tables

- Table 1.1:** Common types of fuel cells with typical fuel utilized, working temperature, electrolyte material, transported ionic species and half reactions.
- Table 1.2:** Thermodynamic data for the reversible oxidation of H_2 , CO and CH_4 at 1 bar and 25 °C.
- Table 2.1:** Plasma etching and magnetron sputtering process parameters used to produce nickel coatings.
- Table 2.2:** Geometric parameters of the four patterned Ni anodes. The section of the trace that is within the outline of the cathode is included in the calculation of l_{TPB} , and A_{Ni} .
- Table 2.3:** Experimental conditions for the various phases of the experiments reported in this study.
- Table 2.4:** Parameters of the experimental periods and experimental timeline for each MEA reported in this study.
- Table 3.1:** Additional TPB length from 5 samples of pattern edges as calculated by the methodology described in section 2.1.2.
- Table 3.2:** Profilometry data of the patterned anodes from MEA 3 (before heat treatment) and MEA 2 (after heat treatment).
- Table 4.1:** Current drawn by the polarized anode (100 μm) from MEA 1 after open circuit and polarization conditions for each experimental period.
- Table 4.2:** Profilometry data of anodes from before any testing (MEA 3) and after electrochemical testing (MEA 1 and 2).
- Table 6.1:** Current drawn by the polarized anode (50 μm) from MEA 3 after open circuit conditions and polarized conditions
- Table 6.2:** Profilometry data of the anodes from before (MEA 3) and after (MEA 4) experimental testing.

List of Figures

Figure 1.1: Schematic of a fuel cell showing its four main parts: an electrolyte, two porous electrodes (anode and cathode), and an external electron conductor.

Figure 1.2: Schematic of a single SOFC MEA operating on H_2/O_2 .

Figure 1.3: Schematic of an MEA with channel flow directing structures assembled in a planar SOFC stack (cathode and electrolyte enlarged for ease of visualization).

Figure 1.4: Representative cell voltage vs. current (or $V-i$) curve for an SOFC.

Figure 2.1: Schematic of the four patterned Ni anodes, two Ni reference electrodes and outline of the cathode.

Figure 2.2: Schematic of photolithographic mask design detailing patterned Ni anodes, traces and Ni pads. Outline of cathode as well as outline of sealing gaskets shown as dotted lines; example anode lead placements are also shown.

Figure 2.3: Representative MEA detailing the four Ni patterns and two Ni reference electrodes (dark circle seen in the center of the translucent electrolyte is the cathode which resides on the far side of the electrolyte).

Figure 2.4: Anode side of MEA 1 detailing a flattened gold lead fixed to a reference electrode via needle tip as well as the attachment of the other pattern's gold leads to the electrolyte via ceramic paste.

Figure 2.5: Anode side of typical MEA showing all leads and gaskets attached via ceramic paste.

Figure 2.6: Cathode side of MEA detailing cathode lead attachment, gold ink electron supply grid, gaskets, and thermocouples.

Figure 2.7: Experimental setup showing home made stand, furnace and compression rig, the red square inset is blown up in Figure 2.8.

Figure 2.8: Inset from Figure 2.7 showing a detail of a loaded MEA and alumina tubes supported by the furnace.

Figure 2.9: Schematic of compression rig with inset of loaded MEA and rubber cork end cap.

Figure 2.10: MEA wiring configurations a) 3-probe, b) 2-probe.

Figure 2.11: Sample EIS plot showing area-specific impedance with excitation frequency (ω) increasing from right to left as shown. Area-specific bulk resistance (R_b) and polarization resistance (R_p) are also indication in the plot.

Figure 3.1: Optical microscope picture (10X magnification) of MEA 2 after heat treatment; the digitally added red boxes show areas photographed for figures presented in this study as numbered.

Figure 3.2: Optical microscope pictures (60X magnification) of the anodes from MEA 1 taken after anode fabrication: a) 10 μm anode, b) 25 μm anode, c) 50 μm anode and d) 100 μm anode.

Figure 3.3: SEM micrograph of a 100 μm patterned anode taken just after microfabrication. The 100 μm scaled overlaid shows that specified pattern geometry was achieved.

Figure 3.4: SEM micrographs (3450X magnification) of TPB regions from different pattern edges just after microfabrication a) 10 μm b) 25 μm c) 50 μm and d) 100 μm . Dark colored streaks radiating from the TPB was due to charging effects.

Figure 3.5: Optical microscope pictures (60X magnification) of the 100 μm anode from MEA 2 a) before heat treatment (with dark material being residual photoresist) and b) after heat treatment.

Figure 3.6: Magnified view of anode geometry with red lines showing the path the profilometer's stylus took when sampling anode profiles.

Figure 3.7: Representative anode profiles from a) MEA 3 before heat treatment and b) MEA 2 after heat treatment.

Figure 4.1: Post-experimental SEM micrographs (3600X magnification) from MEA 2 of a) the open circuit 100 μm pattern edge, b) the 50 μm pattern edge after 8 hrs of polarization ($\eta = 200$ mV) and c) the open circuit 25 μm pattern edge.

Figure 4.2: Profilometry results from a) MEA 3 just after anode fabrication, b) MEA 1 after electrochemical testing and c) MEA 2 after electrochemical testing. Scan paths are shown in Figure 3.6.

Figure 4.3: Impedance curves for the open circuit (10 μm) and polarized (50 μm) patterns from MEA 2 before and after electrochemical testing ($\eta = 200$ mV for 8 hr).

Figure 4.4: $V-i$ curves (with $I \cdot R_b$ subtracted) of the open circuit (10 μm) and polarized (50 μm) patterns from MEA 2 before and after electrochemical testing ($\eta = 200$ mV for 8 hr).

Figure 5.1: Impedance curves of the polarized (100 μm) and open circuit (10 μm) patterns from MEA 5 before and after electrochemical testing.

Figure 5.2: $V-i$ curves (with $I \cdot R_b$ subtracted) for the polarized (100 μm) and open circuit (10 μm) patterns from MEA 5 before and after electrochemical testing.

Figure 5.3: EDAX pattern from the center of a Ni strip from the polarized pattern (100 μm) from MEA 5 after electrochemical testing.

Figure 5.4: Raman data of the polarized pattern (100 μm) from MEA 5 post-electrochemical testing.

Figure 5.5: X-ray pattern from the center of a Ni strip from the polarized pattern (100 μm) from MEA 5 after electrochemical testing.

Figure 5.6: Low magnification (1670X magnification) SEM micrograph of the polarized anode (100 μm) from MEA 5 after electrochemical testing.

Figure 6.1: Impedance curves of the polarized (25 μm) and open circuit (10 μm) patterns from MEA 4.

Figure 6.2: $V-i$ curves (with $I \cdot R_b$ subtracted) of the polarized (25 μm) and open circuit (10 μm) patterns from MEA 4.

Figure 6.3: EDAX results from the current collector bar of the polarized pattern (50 μm) from MEA 3.

Figure 6.4: Raman of the current collector bar from the polarized pattern (50 μm) from MEA 3.

Figure 6.5: Anode profiles a) before electrochemical experiment (MEA 3) and b) after electrochemical experiment (MEA 4). Scan paths are shown in Figure 3.6.

Figure A.1: Optical microscope pictures of a) nickel spot near the 25 μm anode (MEA 1), b) line break in the 25 μm anode (MEA 3) and c) two line breaks of the 10 μm anode (MEA 2).

Chapter 1: General Introduction

1.1 Introduction to Fuel Cells

A fuel cell is an electrochemical device that converts the chemical energy released from a reaction between a fuel and oxidizer directly into electrical energy. The fuel cell accomplishes this by separating the overall reaction into two half reactions each occurring on opposite sides of an ion-conducting, electronically-insulating membrane. The two reactions on each side of the membrane are 1) the oxidation of a fuel at the anode for electron release and 2) the reduction of an oxidizer at the cathode for electron reception. The overall reaction involving the oxidation of the fuel can be used to sustain a voltage difference across the membrane and the resulting electronic current flow through an external circuit will produce electrical work as shown in Figure 1.1.

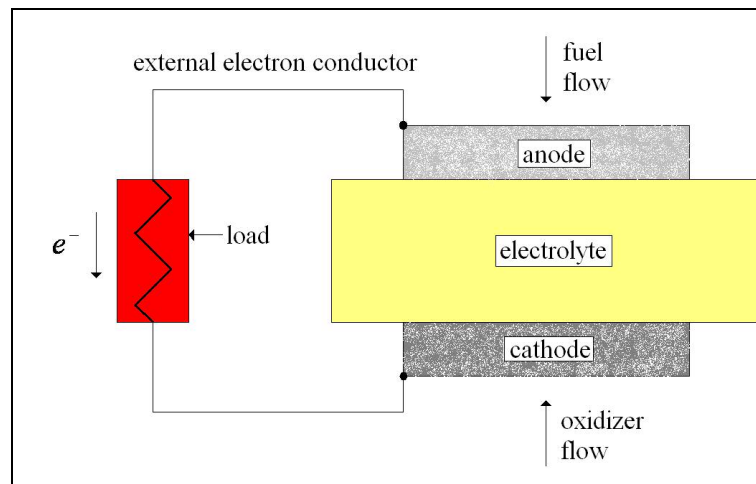


Figure 1.1: Schematic of a fuel cell showing its four main parts: an electrolyte, two porous electrodes (anode and cathode), and an external electron conductor.

Figure 1.1 shows the main components of a fuel cell: an electrolyte (or ionic-conducting membrane), two porous electrodes (an anode and a cathode), and an external electric current conductor. The porous electrodes are usually structures containing electrolyte and electrocatalyst materials. The region where reactant, electrocatalyst and electrolyte meet is termed the three phase boundary (TPB) and it is in this region that charge transfer reactions occur that involve the movement of ions from one phase to another.¹⁻³ Gas-phase reactants must diffuse from the bulk flow into the porous electrode and to the TPB to participate in the charge transfer reactions. Whereas the electrons and ions that participate in the charge transfer reactions at the TPB are either supplied or removed (depending on the electrode and type of fuel cell) via conduction through the electrocatalyst and electrolyte materials, respectively. The combination of the anode/electrolyte/cathode shown in Figure 1.1 make up what is often referred to as a membrane electrode assembly (MEA). A single MEA will in general be incorporated into flow-directing structures which provide the reactant flow over the surface of the two electrodes and collect/distribute electronic current. MEA's and their flow structures are often stacked or wired in series such that the voltages produced by each cell can be summed yielding a greater voltage across the overall stack.

For the fuel cell to produce electric work, the cathode must sustain a higher potential relative to the anode. This is achieved as voltage losses associated with driving a current flow are less than the electric potential difference created by the free energy change of the two-combined half reactions. The external load will determine the

demand for external electronic flow wherein the voltage drop across the load equals the voltage available after internal losses in the fuel cell.

The electrodes are in contact with opposite sides of the electrolyte and they participate in the oxidation and reduction charge transfer reactions that liberate electrons at the anode and consume electrons at the cathode, respectively. The electrolyte electronically isolates the anode from cathode - thereby forcing the electrons to flow through an external conductor (or in stacks of MEA's to or from the adjacent MEA). The electrolyte also physically separates the fuel and oxidizer preventing them from undergoing spontaneous non-electrochemical reactions. The ionized species produced at either the anode or cathode depend on the type of fuel cell electrolyte and what ionic species the electrolyte can conduct to an opposing electrode where it is consumed thus completing the path of charge flow. The chemical potential gradients across the electrolyte drive the ionized species across the electrolyte and into the porous structure of the electrodes.

There are five commonly known types of fuel cells and they are named based on the composition of the electrolyte they utilize. They all operate based on the principle of converting chemical energy directly into electrical energy. However, they differ in form, materials used, working temperature, and ionic species conducted through the electrolyte. These five types are listed in Table 1.1 along with typical fuels utilized, working temperature, electrolyte material, transported ionic species and half reactions.

Table 1.1: Common types of fuel cells with typical fuel utilized, working temperature, electrolyte material, transported ionic species and half reactions.⁴

Fuel Cell	Fuel	Working Temp [°C]	Anode Half Reaction	Electrolyte Material / Transported Ionic Species	Cathode Half Reaction
Alkaline Fuel Cell (AFC)	H ₂	~ 250	$H_2 + 2OH^- \rightarrow 2H_2O + 2e^-$	KOH / OH ⁻	$1/2 O_2 + H_2O + 2e^- \rightarrow 2OH^-$
Molten Carbonate Fuel Cell (MCFC)	CH ₄ , coal	~ 650	$H_2 + CO_3^{2-} \rightarrow H_2O + CO_2 + 2e^-$ $C + CO_3^{2-} \rightarrow 2CO_2 + 2e^-$	Molten alkali metal carbonates retained in LiAlO ₂ matrix / CO ₃ ²⁻	$1/2 O_2 + CO_2 + 2e^- \rightarrow CO_3^{2-}$
Phosphoric Acid Fuel Cell (PAFC)	CH ₄ , CH ₃ OH	150 – 225	$H_2 \rightarrow 2H^+ + 2e^-$	H ₃ PO ₄ / H ⁺	$1/2 O_2 + 2H^+ + 2e^- \rightarrow H_2O$
Polymer Electrolyte Membrane (PEM)	H ₂ , CH ₃ OH	50 – 100	$H_2 \rightarrow 2H^+ + 2e^-$	Nafion (® Dupont) (fluoroethylene) / H ⁺	$1/2 O_2 + 2H^+ + 2e^- \rightarrow H_2O$
Solid Oxide Fuel Cell (SOFC)	H ₂ , CO, CH ₄ , coal	600 – 1000	$H_2 + O^{2-} \rightarrow H_2O + 2e^-$ $CO + O^{2-} \rightarrow CO_2 + 2e^-$ $CH_4 + 4O^{2-} \rightarrow 2H_2O + CO_2 + 8e^-$	YSZ / O ²⁻	$1/2 O_2 + 2e^- \rightarrow O^{2-}$

Fuel cell electrolytes can exist in the liquid phase as is the case for the alkaline, molten carbonate, and phosphoric acid fuel cells or the electrolyte can be a solid as in the polymer electrolyte or the ceramic-based solid oxide fuel cells. When the electrolyte exists as a liquid a supporting matrix is used, e.g. the molten carbonate fuel cell uses a porous lithium aluminate matrix. The electrolyte composition determines the ionic species that is conducted between electrodes, e.g. the electrolyte of the solid oxide fuel cell is a ceramic material that is doped with oxides which introduce oxygen vacancies into its lattice structure thereby allowing the conduction of oxide ions (O^{2-}).⁵ The temperature necessary for conduction of ions through the electrolyte largely dictates the operating temperature for the fuel cell. For SOFC's, below the lower operating temperature limit of 600 °C the resistance to O^{2-} transport through the electrolyte becomes too large.

The electrodes in some fuel cells may require noble metal loading to increase their catalytic activity to an acceptable level at low temperatures where the reactions would not otherwise proceed at practical rates. Noble metal loadings also prevent electrode degradation; such is usually the case for phosphoric acid and PEM fuel cells. Higher temperature fuel cells can use metals or semiconductor materials as electrocatalysts: e.g. the molten carbonate fuel cell can utilize a nickel-chromium alloy as an anode catalysts and similarly the high temperature SOFC can utilize nickel as an anode catalyst and perovskite ceramics for cathode catalysts.⁶ The higher operating temperatures of SOFC's necessary for O^{2-} conduction gives them the potential to operate on heavy hydrocarbons, without the need for expensive noble metal loading,

as suggested by the anode half reactions listed in Table 1.1. At these high temperatures hydrocarbon fuels break down into smaller fuels that can be directly electrochemically oxidized. It is this possibility of stable operation with hydrocarbons and other carbonaceous fuels that in part motivates the current study on the stability of Ni anodes in SOFC's.

1.2 The Solid Oxide Fuel Cell

The SOFC can be distinguished from other fuel cells by the fact that it utilizes a dense ceramic electrolyte. Hydrogen/air is a common fuel/oxidizer pair for SOFC's. The O_2 from the air is reduced at the cathode to O^{2-} and is conducted across the solid ceramic electrolyte to the anode where it reacts with H_2 to produce H_2O . The electrons liberated in the H_2 oxidation reaction travel through the external electron conductor to the cathode to reduce the O_2 . A schematic of a single SOFC MEA operating on H_2/O_2 is shown in Figure 1.2. The global half reactions that occur at each porous electrode's TPB are shown in Figure 1.2 with the phase of the species in parentheses (a = anode, c = cathode, el = electrolyte).

The most common geometries for the SOFC are the tubular and planar geometries.⁷ In state of the art tubular geometries the supporting structure is tubular and may be a thick (on the order of 1.0 mm) porous anode. The electrolyte and fuel electrode are then deposited on the outside of this tube. Typically one end of this tube is closed and the fuel is injected near the closed end via an alumina tube.⁷ Air is flown around the outside of the tube and the fuel is electrochemically oxidized at the anode as it

nears the open end. Some of the exhaust fuel is re-circulated into the fuel stream and the remaining fuel is burned with the oxygen-depleted air in a downstream combustor to preheat incoming flows.

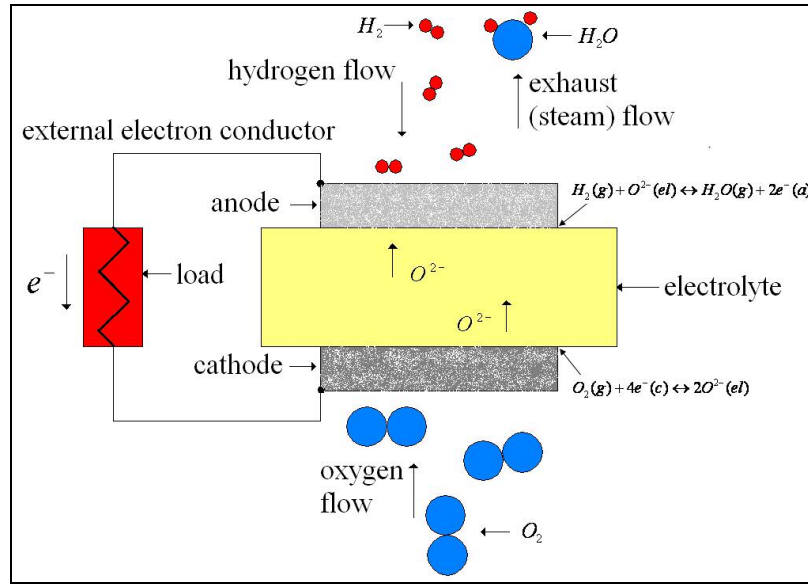


Figure 1.2: Schematic of a single SOFC MEA operating on H_2/O_2 .

In the planar configuration, the electrodes and electrolyte are flat and stacked on one another. The voltage generated by a state-of-the-art MEA (operating on wet H_2 at 800 °C) when drawing maximum current ($\sim 3.5 \text{ A/cm}^2$) is around 0.4 volts.⁸ As mentioned in section 1.1 to increase this voltage to a useable level individual MEAs are arranged in an electrical series configuration in what is called a fuel cell stack as shown in Figure 1.3 (components are not drawn to scale).

Typically the anode is the support structure of the MEA and a thin electrolyte and cathode are deposited or tape cast onto the anode. The design tradeoff to be met with

planar SOFC's is between fabricating thin electrodes and electrolytes that minimize diffusion and ionic transport losses while at the same time maintaining a structure thick enough for rugged performance.

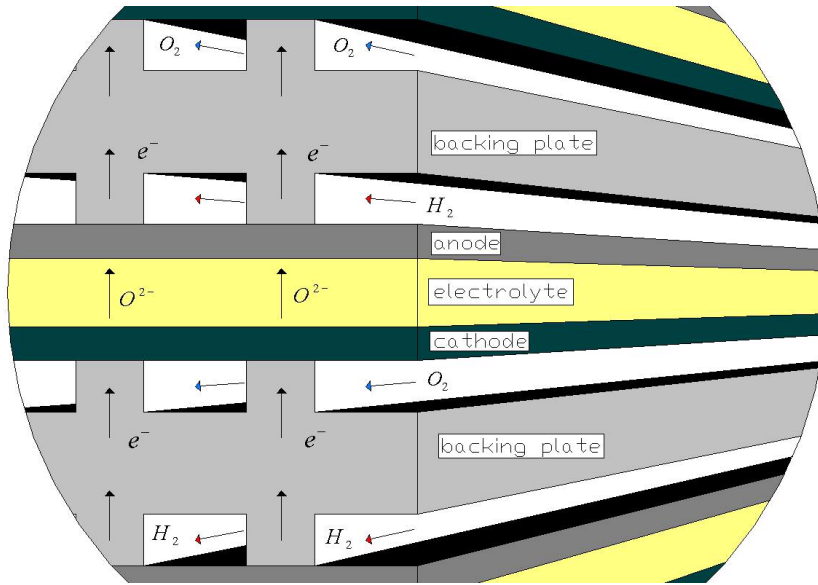


Figure 1.3: Schematic of an MEA with channel flow directing structures assembled in a planar SOFC stack (cathode and electrolyte enlarged for ease of visualization).

A backing or bipolar plate is placed between all cells in the stack and isolates the fuel flows from the oxidizer flows between MEA's while simultaneously providing structural support to the system. The backing plates' channel structures direct the flows over the MEAs' external surfaces and also functions as an electronic interconnect conducting electrons produced at the anode of one MEA to the cathode of the adjacent MEA. A common SOFC backing plate material is doped lanthanum chromite which has a high electronic conductivity in both reducing and oxidizing atmospheres at the high temperatures required for satisfactory SOFC operation.⁹ The

power the stack provides can be increased by utilizing electrodes with interwoven structures of pores, electrolyte and electrocatalyst that have a large amount of TPB length. As mentioned in section 1.1 the charge transfer reactions occur at the TPB and increasing its length will increase the amount of current the MEA can produce. Often the current scales with the geometric area of these ceramic-metal (cermet) electrodes and is reported as a current density with units [A/cm^2].

The operational temperature of state-of-the-art SOFC's ranges between 600 °C and 1000 °C and is necessary for the conventional yttria-stabilized zirconia (YSZ) electrolytes to provide adequate O^{2-} ion conduction without significant ohmic overpotentials well as electronic insulation. Operation of YSZ electrolyte fuel cells becomes impractical below 600 °C because the resistance to O^{2-} transport through electrolytes of thicknesses as low as a few microns is too large and above 1000 °C system components break down quickly and the heat requirement of the system becomes large.

Most SOFC systems operate at near atmospheric pressure, save the SOFC/gas turbine hybrid system, which operates between 3 and 30 times atmospheric pressure.

Originally, SOFC's were designed for large power applications, such as replacing diesel engines on ships and trains, but they can also be used as stationary combined heat and power sources or automotive auxiliary power devices.⁷ SOFC's are being developed to operate directly on carbonaceous fuels and in particular for ≤ 1 kW applications where liquid fuel capabilities are critical for mobile power applications.⁸

¹⁰⁻¹² The ability of the SOFC to operate directly on hydrocarbons eliminates the need for a fuel pre-processor system and allows the SOFC to more easily integrate into the existing fuel infrastructure. In the high temperature anode chamber heavy hydrocarbons can be reformed (either with added water or product water) into mixtures of H₂, CO, CH₄, and other lighter hydrocarbons which can then be electrochemically oxidized at the anode.¹³ CO and CH₄ electrochemical oxidation on cermet Ni anodes have shown to be sustainable when mixed with steam (for a steam to carbon ratio > 2) or when an adequate oxide ion flux is provided to the anode through the electrolyte.¹¹ However, without added water hydrocarbon fuel feeds undergo pyrolysis and carbonaceous deposits form that have shown to seriously degrade Ni anode performance.^{11, 14, 15} Ni catalyses the formation of carbon fibers and if insufficient steam is present or oxide ion flux is inadequate even with the lighter fuels (CO and CH₄) these carbon deposits can push Ni particles apart decreasing the anode's conductivity and block otherwise active electrochemical sites.^{7, 15, 16} The electrochemical reactions of dry hydrocarbons at the Ni anode are less certain and there is significant discussion in the SOFC literature over the actual electrochemical reactions that describe the oxidation of these fuels.^{10, 13, 14, 17, 18}

Much of the uncertainty in SOFC surface chemistry remains because studies conducted on commonly-used cermet Ni/YSZ anodes cannot tie kinetic information directly to the parameters of the anode's microstructure. In these cermet anodes the exact microstructure, i.e. the length of TPB per unit volume and amount of electrochemically active sites is very difficult to quantify. To overcome this,

patterned anodes on YSZ electrolytes can provide a greater understanding of the relationship between the anode's microstructure and the rate limiting steps occurring at the anode.¹⁻³ However, knowledge of the structure of patterned Ni anodes operated in SOFC environments is critical for interpreting electrochemical data collected using such anodes. Therefore, the stability and behavior of patterned Ni anodes operated at SOFC conditions is the basis for the current study which stands as a preliminary effort to understand direct electrochemical oxidation of heavier hydrocarbon fuels.

1.2.1 SOFC Materials

A major challenge in SOFC development involves long-term durability of electrode materials for operation with the various fuels of interest including H₂, CO, and CH₄. The anode and cathode components of the SOFC require different materials based upon their need to resist chemical attack in the reducing and oxidizing environments respectively. Furthermore, both electrode components must be chemically and thermomechanically compatible with the electrolyte material with which they are intermixed in the porous region near the dense electrolyte layer. Mixing electrolyte particles with electrocatalyst particles increases electrode performance by increasing TPB length and it also helps the electrode adhere to the electrolyte. Finding the proper mixture of metal and ceramic for the cermet electrodes is important because the temperature cycling that a practical fuel cell would undergo (due to start up and shut down) makes it difficult to connect these materials, which have significantly different coefficients of thermal expansion (CTE's).¹⁶

Another SOFC materials challenge is sealing around the electrolyte. Leakage of reactant gases across the electrolyte creates a drop in cell potential due to mixing of the fuel and oxidizer at high temperatures and subsequent exothermic non-electrochemical reactions that convert all of the chemical energy into heat. Further complicating the problem is the fact that thin cell components that are desirable because they reduce voltage losses within the cells are more prone to fracture especially due to forces arising from thermal expansion. The integrated cell components in an MEA must resist thermally induced stress that may occur during emergency shut down or quick start-up demands.

An electrolyte that displays good performance will have the following characteristics:

- High ionic conductivity and minimal electronic conductivity
- Low permeability to reactant gases
- High resistance to fracture and thermal shock
- Stability in oxidizing and reducing atmospheres at temperatures < 1000 °C
- A CTE very close to the CTE's of other cell components

The most common electrolyte material is yttria stabilized zirconia (YSZ), which has been adapted in all demonstration SOFC systems to date and will be used in the current study. Samples having densities of more than 94 % that of the theoretical density have adequately low leakage rates for operation of SOFC MEA's.¹⁹ The yttria, Y_2O_3 , doping stabilizes the fluorite structure of the zirconia, ZrO_2 , down to room temperature and the vacancies in the oxide structure created by the yttria enhances conduction of the oxide ions. Typically the yttria is added at a 8 – 10.5%

molar ratio (13 – 16 % by weight) to give a fully stabilized cubic material.⁷ Calcia, magnesia and scandia can also be used as zirconia dopants to enhance ion conduction.^{5,7} YSZ is a good electrolyte material because it is abundant, chemically stable, non-toxic, readily processed, and relatively fracture resistant. The main drawbacks are 1) the high temperatures (> 600 °C) for good O²⁻ conductivity and 2) the difference between the CTE of YSZ (~11 *10⁻⁶ [°C⁻¹]) and other cell components, which creates joining and sealing difficulties.

A cathode that displays good performance must meet the following criteria:

- Stable in an oxidizing environment and at temperatures < 1000 °C
- Electronic conductivity of at least 50 [$\Omega^{-1}\text{cm}^{-1}$]¹⁹
- Porosity of 30 %¹⁹
- Exhibits good activity for oxygen reduction
- CTE that matches other cell components

Base metals are not viable electrocatalyst materials because they cannot withstand the high temperature oxidizing environments⁷ nor are noble metals because they are cost prohibitive, thus developers have focused semi-conductor materials for most applications. Strontium-doped lanthanum manganite, $\text{La}_{1-x}\text{Sr}_x\text{MnO}_{3-\delta}$ (LSM), is a commonly used perovskite material for cathode electrocatalyst. It is implemented in the current study because it has been well-characterized and thus the focus on anode kinetics is facilitated. LSM is stable in oxidizing environments up to 1100 °C and has an electronic conductivity of 80 [$\Omega^{-1}\text{cm}^{-1}$] at this temperature.¹⁹ Increasing the strontium doping level (up to 0.5) increases electronic conductivity²⁰, but adjustment

of mixture stoichiometry and powder characteristics must be met to yield a CTE and porosity that match other cell components. In this study LSM and YSZ powders were mixed in a 50/50 ratio to balance electronic conductivity, increased TPB length and adherence of the cathode to the electrolyte.⁷

For the anode electrode, metallic nickel is the most common anode electrocatalyst because of its high activity for H₂ oxidation at high temperatures and because of its relatively low cost in comparison to precious metals. To provide high amounts of TPB length in the electrochemically active region, Ni/YSZ cermets are used to form a porous structure with high activity for fuel oxidation and good transport of O²⁻ to the TPB regions. A good anode must meet the following criteria:

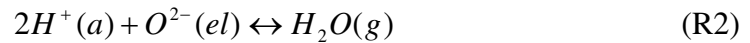
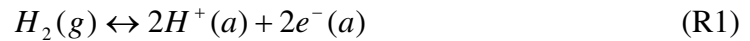
- Stability in a reducing environment at temperatures < 1000 °C
- Electronic conductivity of at least 120 [$\Omega^{-1}\text{cm}^{-1}$]¹⁹ at operating temperatures
- Catalyst for electrochemical oxidation of a range of fuel compositions
- CTE that matches other cell components ($\sim 13 \cdot 10^{-6} [^{\circ}\text{C}^{-1}]$)⁷

A minimum of 30 vol.% nickel is required to meet the electronic conductivity requirement.¹⁶ Small particles of nickel are dispersed throughout the YSZ structure containing coarse and fine YSZ particles. The coarse YSZ particles give the anode a CTE that more closely matches the electrolyte, prevent significant agglomeration of the Ni particles, and retains a microporous structure, while the fine YSZ particles bind the structure together. The electrochemical performance of Ni/YSZ anodes depends on this microstructure and improvement of the microstructure has been mostly accomplished by empirical investigations because the exact reaction

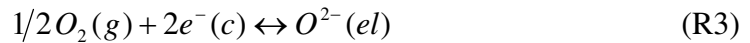
mechanisms and anode kinetics are not fully understood even for electrochemical oxidation of simple fuels like H_2 .^{1,9} As mentioned in section 1.2 a significant drawback of Ni/YSZ anodes is their propensity to form carbonaceous deposits when operating directly on carbonaceous fuels and it is not clear yet whether Ni catalyst can be used for long term operation on carbon containing fuels without addition of a significant amount of steam.²¹ It is desirable to further lower the losses associated with Ni anodes and improve the long term stability and durability of Ni anodes in hydrocarbon fuel feed environments.

1.2.2 SOFC Performance

To determine the working voltage of a given SOFC MEA it is useful to define the electrochemical potential difference that is related to the maximum (reversible) work that can be provided from the free energy change of the reversible half reactions. For an SOFC operating on H_2 and O_2 , H_2O is produced at the anode by the following reversible reactions where the parentheses indicate the phase of the species (g = gas phase, a = anode, c = cathode, el = electrolyte).



At the cathode, oxygen is reduced.



The reversible change in the enthalpy in going from the un-mixed reactants to unmixed-products of (R1) and (R3) must balance the heat transported from the cell and the work delivered by the cell.²²

$$\Delta H_{rxn} = Q_{rev} + W_{rev} \quad (1.1)$$

And the transport of reversible heat to the environment must be compensated for by the reaction entropy.²²

$$Q_{rev} = \Delta S_{rxn} * T \quad (1.2)$$

Combining equations (1) and (2) with the expression for electrical work yields

$$W_{rev} = \Delta H_{rxn} - T * \Delta S_{rxn} = \Delta G_{rxn} = -n_{elec} F V_{rev} \quad (1.3)$$

where n_{elec} is the moles of electrons transferred per mole of reaction, F is Faraday's constant (96,485 C/mole of electrons) and V_{rev} is the reversible voltage of the cell.

The change in Gibbs free energy for the reaction ΔG_{rxn} is a function of temperature and pressure and since the pressures are relatively low and the temperatures high in SOFC's, the reactants and products can be assumed to obey the ideal gas law. Thus the Gibbs free energy of the combined two half reactions can be written as

$$\Delta G_{rxn}(T, P) = \Delta G_{rxn}(T) + T * R_u * \ln(K) = \Delta G_{rxn}(T, P^o) + T * R_u * \ln\left(\prod_k \left(\frac{P_k}{P^o}\right)^{v_k}\right) \quad (1.4)$$

The second term on the right hand side of equation 1.4 is the dependency of entropy on pressure. R_u is the universal gas constant, K is the equilibrium constant of the oxidation reaction and v_k are the stoichiometric coefficients for each species in the global oxidation reaction. Table 1.2 gives the change in enthalpy, entropy, and Gibbs free energy for the reversible oxidation of H₂, CO and CH₄ at standard conditions.

Table 1.2: Thermodynamic data for the reversible oxidation of H₂, CO and CH₄ at 1 bar and 25 °C.

Fuel	$\Delta H^\circ_{\text{rxn}}$ (kJ/mol)	$\Delta S^\circ_{\text{rxn}}$ (J/mol*K)	$\Delta G^\circ_{\text{rxn}}$ (kJ/mol)
H ₂	- 241.8	- 44.3	- 228.5
CO	- 282.9	- 86.4	- 257.2
CH ₄	- 802.3	- 5.1	- 800.6

The maximum available work a cell can provide is achieved when the cell temperature and partial pressure of reactants is fixed and no net current flows through the cell. Under these conditions the potential difference between the cell's electrodes achieves its maximum value and is termed the open circuit voltage (OCV). When current is drawn from the cell the electrodes are said to be polarized and irreversibilities arise that cause the available work (i.e. cell voltage) to be reduced.

$$W_{act} = n_{elec} F V_{act} = n_{elec} F V_{rev} - n_{elec} F \sum_j \eta_j = W_{rev} - W_{lost} \quad (1.5)$$

$$V_{act} = \frac{W_{act}}{n_{elec} F} = V_{rev} - \sum_j \eta_j \quad (1.6)$$

The η_j 's are the voltage losses or overpotentials that arise due to the irreversibilities associated with the flow of current. Figure 1.4 shows a representative voltage vs. current (or $V-i$) curve for an SOFC. The point where the dashed lines intersect represents an operating point for the SOFC on the $V-i$ curve and at this point η_j is the difference (in volts) between the cell's OCV and the cell's working voltage.

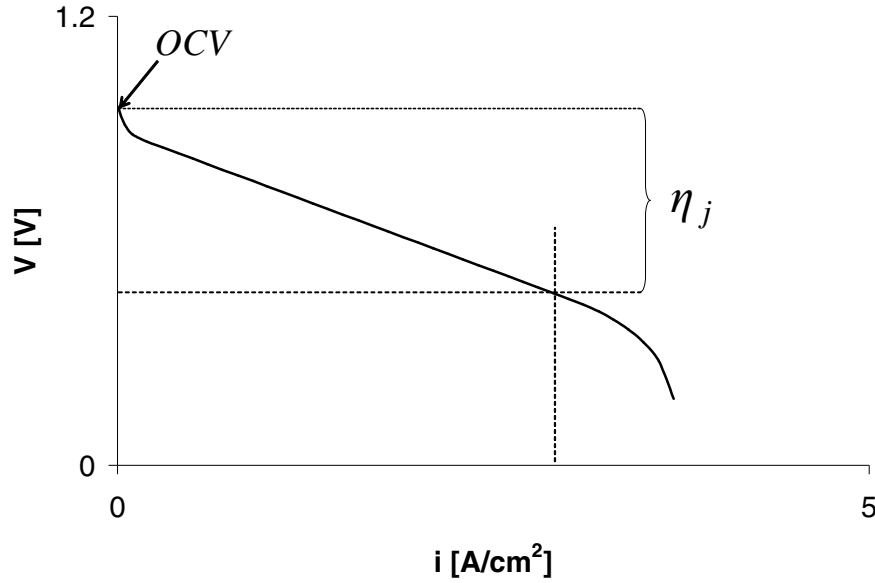


Figure 1.4: Representative cell voltage vs. current (or V - i) curve for an SOFC.

There are three different types of overpotentials named in reference to the underlying irreversible phenomena that cause them, they are: concentration overpotential (η_{conc}), ohmic overpotential (η_{ohm}) and activation overpotential (η_{act}). All three overpotentials associated with both electrodes act to decrease the available cell voltage along the entire V - i curve. However, at high currents η_{conc} dominates the drop in cell voltage, at midrange currents η_{ohm} dominates and at low currents η_{act} dominates the drop in voltage.

At very high currents electrochemical reactions process reactants faster than new reactants can replace them and the cell's voltage sharply decreases. In reality η_{conc} is a drop in V_{rev} due to a drop in the local partial pressure of the reactants at the electrode/electrolyte interfaces and thus a change in the pressure term in the ΔG_{rxn} .

However, it is often modeled as an overpotential because ΔG_{rxn} is often calculated using the channel flow conditions. For cermet electrodes η_{conc} is large when diffusion to the electrochemically active sites is impeded i.e. for thick electrodes with low porosity and high tortuosity.

At moderate currents the resistance to the associated electronic and ionic flows dominates the cell's voltage loss. In this region the voltage-current relationship is approximately linear as shown in the middle of the $V-i$ curve in Figure 1.4. η_{ohm} includes the electrodes' resistance to electron motion, the electrolyte's resistance to ion motion, and any interfacial resistances between current collector / electrode and electrode / electrolyte interfaces. For cells that have good contact between electrodes and electrolyte the ohmic resistivity of the electrolyte is the main contributor to η_{ohm} (YSZ $\sim 50 \Omega\text{cm}$ at 800°C).⁷

Activation overpotential results from the energy required to activate the charge transfer processes that occur at the electrodes. Equation (6), known as the Butler-Volmer equation, gives a qualitative relationship between η_{act} and current density that is applicable for low cell currents.²³

$$i = i_o \left[e^{\alpha F \eta_{act} / RT} - e^{-(1-\alpha) F \eta_{act} / RT} \right] \quad (1.7)$$

In equation 1.7 i_o is the so-called exchange current density, which is the magnitude of the current, positive or negative (associated with the forward and backward reactions), at an electrode in equilibrium. At small η_{act} the current density can be approximated to be a linear function of overpotential. The ratio of overpotential to

current density is called the charge transfer resistance of the cell (R_{CT}) and is given by equation (1.8).

$$\left. \frac{\eta_{act}}{i} \right)_{\lim i \rightarrow 0} = R_{CT} = \frac{RT}{Fi_o} \quad (1.8)$$

R_{CT} is the initial slope of the $V-i$ curve (Figure 1.4) and is a measure of the performance of the electrodes. For larger positive η_{act} the first term in equation (1.7) dominates and the overpotential varies with the natural logarithm of current density. The information contained in the response of an electrode to activation overpotentials is useful for understanding the kinetics of that electrode, including the reactions taking place on the electrode, the rates of these reactions and the species involved. An understanding of the reaction mechanism occurring at electrodes will make possible further improvements in electrode performance.

1.3 Patterned Anodes for Understanding η_{act} and SOFC Kinetics

Previous research on Ni cermet anodes varied partial pressure of reactants and anode overpotentials to study anode kinetics.²⁴⁻²⁷ However, the results of these studies could not be linked to anode microstructural parameters, such as length of TPB, because these parameters are not easily quantified.²⁸ In addition, the degree to which diffusion through the porous anode and heterogeneous chemistry influences the electrochemical oxidation processes remains unknown. The approximately 2-dimensional structure of the pattern anodes eliminates the effect of diffusion of reactants through a porous structure as well as the effect of heterogeneous chemistry occurring at non-electrochemically active sites. The microstructure can be

characterized in terms of length of TPB, surface area of Ni exposed to the fuel atmosphere, and area of contact between Ni and YSZ. These microstructural parameters of the anode can then be related to their electrochemical performance and can lend insight into what mechanisms take place during the electrochemical oxidation of various fuel and what steps in these mechanisms are rate limiting.

Studies of pattern Ni anodes operating on humidified H₂ have been completed but the results have not brought about a clear consensus on anode reaction mechanisms.^{1-3, 14, 28} One study proposed that water hydroxylates the YSZ surface allowing conduction of H⁺ protons across the YSZ there by extending the effective TPB region.²⁸ Others have proposed that adsorbed intermediates play an active role in the electrode process¹ or that the rate limiting step of the mechanism occurs on the Ni surface between hydrogen and absorbed oxygen atoms.² However, most studies find that anode performance directly scales with length of TPB. More research in this area is required to elucidate the exact electrochemical oxidation mechanisms of H₂ as well as other important fuels (CO and CH₄).

It is desirable that SOFC's with Ni-based anodes sustain operation on hydrocarbon fuel feeds because 1) Ni is a relatively cheap electrocatalyst and 2) our existing fuel infrastructure is well suited for liquid hydrocarbons fuels. Experiments involving electrochemical oxidation of H₂, CO and CH₄ on patterned Ni anodes can lead to an understanding of the performance of SOFC's on hydrocarbon fuel feeds. As discussed in section 1.2 heavy hydrocarbon fuel feeds can be reformed, either through

external reforming or internal reforming (via. added or product water) into mixtures of H_2 , CO, CH_4 and other lighter hydrocarbons. Simultaneous testing of multiple Ni pattern anodes operating on H_2 , CO and CH_4 that have well defined but differing geometries can lead to quantifying rate-limiting elementary kinetics which could then be connected to global electrochemistry. It can also provide information on the extent of direct hydrocarbon oxidation in Ni-based anodes and the role of CO and CH_4 in electrochemical oxidation of pre-reacted mixtures. This information can lead to identifying under what conditions, if any Ni-based anodes can sustain operation on hydrocarbon fuel feeds.

1.4 Objectives of the Current Study

To properly interpret electrochemical data collected using patterned Ni anodes, the structure and the stability of the patterned anodes must be characterized under the various experimental operating conditions. This characterization provides a solid basis for evaluating how the performance of each electrode varies in light of their differing geometries. Knowing the behavior of the patterns also allows the translation of electrochemical measurements into fundamental data which can be used to evaluate kinetic models. Preliminary results on patterned Ni anodes operating on H_2 and CO suggested that reaction rates did not scale with TPB length as has been seen in the literature but rather with Ni/YSZ contact area for pattern widths less than 100 μm .¹⁴ Patterned anode fabrication techniques were varied and it was found that SOFC-like conditions caused a structural change in some anodes as discovered through post-experimental analysis. Optical microscopy revealed that for some

patterns the Ni strips had agglomerated into many Ni islands and testing using a multimeter proved that the anodes were electrically discontinuous. To continue study of H₂, CO and CH₄ electrochemical oxidation on pattern Ni anodes the structure of the anodes needed to be more fully characterized and understood. Therefore the objectives of the current study are as follows:

- Establish a Ni deposition and photolithographic procedure for fabricating Ni patterned anodes with characterized TPB length and Ni/YSZ contact area on a cathode/YSZ half cell.
- Characterize the quality of the patterned Ni anodes including their TPB sharpness, Ni surface roughness and adherence to the YSZ as a function of exposure to various reducing environments and electrochemical overpotentials.
- Operate the patterned anodes on humidified H₂, CO and CH₄ fuel feeds at typical SOFC temperatures and anodic overpotentials while making in situ electrochemical measurements to determine the impact of fuel and overpotential on anode stability.

This thesis will first describe the fabrication of the MEA's tested in this study. Then the experimental rig, control of experimental parameters, and the experimental procedure followed during the electrochemical tests will be explained. Next the results of the non-electrochemical and electrochemical testing will be presented and discussed in relation to anode stability. The thesis will then end with conclusions drawn from the experimental results and recommendations for future studies.

Chapter 2: Experimental

To characterize the patterned anodes' structural and electrochemical stability under SOFC conditions four Ni patterns were fabricated on supporting single crystal YSZ electrolytes with high surface area porous cathodes on the opposite side and tested under typical SOFC temperatures and for humidified H₂, CO and CH₄ fuel feeds. One of the four anodes was kept at a typical working overpotential and the other three under open circuit conditions. The stability of the patterns as a function of exposure time was checked using in situ electrochemical impedance spectroscopy and voltammetry measurements. Structural and chemical analysis of the anodes was performed ex situ to elucidate any change in the patterned microstructure and/or chemical species on the Ni surface.

2.1 MEA Fabrication

High surface area porous LSM/YSZ cathodes were tape cast onto one side of the supporting electrolyte and sintered in air followed by deposition of the nickel and subsequent pattern fabrication. Each electrolyte was fully dense, 99.99 % pure, 9 % mole yttria ((Y₂O₃)_{0.09}(ZrO₂)_{0.91}) (MTI Corp.), and for the results reported herein was in the shape of a square 25.4 mm on a side and either 0.5 mm or 1 mm thick.

2.1.1 Cathode Fabrication

The porous LSM/YSZ cathodes were fabricated on the non-polished side of the single crystal YSZ electrolyte to provide good adherence between the dense electrolyte and the porous electrode. The cathode material was a mixture of 50% (by weight) LSM ($\text{La}_{0.85}\text{Sr}_{0.15}\text{MnO}_{3-\delta}$) and 50% YSZ ($((\text{Y}_2\text{O}_3)_{0.08}(\text{ZrO}_2)_{0.92})$) and prepared in a fashion similar to described in the literature.²⁹ In a metal vile, 0.5 g of 50 % LSM and 50 % YSZ and 0.117 g of KD 1 were ball milled for 5 min. Then 0.2740 mL of toluene was then added to the vile to act as a solvent, and the vile was sealed with parafilm to prevent significant evaporation of the toluene during further ball milling for another 5 min. After the vile was allowed to cool to room temperature, 0.325 mL of polyethylene glycol (PEG-600), 0.0432 mL phthalate, and 0.0265 g poly vinyl butyral (PVB) were added and the vile that was again sealed with parafilm. The vile was ball milled for a final 5 min period and then cooled to room temperature. The cathode material came out as a liquid with viscosity comparable to that of vegetable oil. A section of Kapton tape with a hole (12 mm in diameter) was centered on the electrolyte and the cathode material was tape cast onto the electrolyte through this hole. The cathode thickness (before sintering) was estimated to be the thickness of the Kapton tape (50 μm).

The coated liquid cathode solution was dried in air for 20 min then under a heat gun at approximately $60\text{ }^{\circ}\text{C} \pm 5\text{ }^{\circ}\text{C}$ for 2 hrs. The tape template was removed and the cathode was sintered in air according to the following schedule: it was ramped from $25\text{ }^{\circ}\text{C}$ to $400\text{ }^{\circ}\text{C}$ at $0.3\text{ }^{\circ}\text{C}$ per min, held for 1 hr at $400\text{ }^{\circ}\text{C}$. After that, the cathode was

heated from 400 °C to 1300 °C at 3.0 °C per min, and held at 1300 °C for 1 hr before being returned to 25 °C at a rate of 3.0 °C per min.

2.1.2 Anode Microfabrication

After the cathode was prepared, the cell was transferred to a clean room for nickel deposition. The smooth surface of the electrolyte was cleaned of particles and organics by acetone and plasma etching. This smooth polished side was found by profilometry to have a roughness of approximately 0.5 nm before deposition of the Ni film for the patterned anodes. The Ni films were deposited on this polished side so that a sharp, quantifiable TPB could be achieved through the photolithographic fabrication processes. To produce a nickel coating that maintained its continuity and adherence to the electrolyte and was free of pores and cracks different thicknesses of nickel (100 nm, 300 nm, 500 nm and 1 μm) and different coating methods (electron-beam and sputter deposition) were used to fabricate MEA's that were subsequently exposed to SOFC conditions and electrochemical testing. The coatings that performed the best were those with nickel deposited on the electrolyte in approximately a 1 μm thickness via DC magnetron sputtering (AJA International, ATC 1800-V). These coating were completely continuous, free of cracks and pores with diameters $> 0.25 \mu\text{m}$ and mimicked the geometry of the photolithographic mask. The patterns, for the most part, survived high temperature SOFC conditions without causing gross macrostructural changes due to particle agglomeration causing discontinuity as seen in other coatings. These observations were made using ex situ imaging with a scanning electron microscope (SEM) and an optical microscope. The

parameters of plasma etching and sputter deposition processes used to produce the anode coatings of the MEA's reported in this study are listed in Table 2.1.

Table 2.1: Plasma etching and magnetron sputtering process parameters used to produce nickel coatings.

RF Plasma Etching			DC Magnetron Sputtering		
<u>Parameter</u>	<u>Value</u>	<u>Unit</u>	<u>Parameter</u>	<u>Value</u>	<u>Unit</u>
Power	20	W	Power	200	W
DC bias	170	V	Rate	113	Å/min
Chamber Pressure	30	mTorr	Chamber Pressure	5	mTorr
Bath Gas Flowrate	20	sccm N ₂	Bath Gas Flowrate	20	sccm N ₂
Etch Time	5	min	Sputter Time	100	min
Working Distance	111	mm	Working Distance	111	mm

The sputter deposition method and smoothness of the electrolyte surface were critical to achieving a dense and continuous Ni layer free of holes and cracks. It was important to ensure that the nickel patterns were free of holes or cracks so that the additional TPB length beyond the desired patterned boundary length did not significantly influence the electrochemical reaction rates. In future studies on similar MEA's with these patterned anodes, the quantifiable length of TPB will be used in identifying the rate-limiting steps of Ni anode kinetics operating on different fuels.

The process parameters of the photolithographic procedure were tuned in a trail and error fashion using test glass slides with Ni coatings similar to the MEA's in order to repeatability produce high quality patterned anodes. Those process parameters critical to achieving desired anode geometry included the length of time in which the MEA's were submerged in the developing and etching solutions, as well as the

concentration of those solutions. The quality of the patterns (i.e. TPB sharpness) was visually determined using an optical microscope for many different process parameter values and those parameter values that yielded the best patterns on the glass slides were adopted for the MEA fabrication process.

For the eventual selected fabrication method, a photoresist (Microposit S1813, Rohm and Haas) was brought to room temperature then coated on the Ni surface using a spin coater (Headway Research Inc.) at 40,000 rev/min for 40 s. The resist was soft baked on a hot plate held at 90 °C for 1 min. The cell was cooled back to room temperature and then placed in a mask aligner (MJB3 Mask Aligner, Karl Suss) and brought into contact with a custom made chrome-patterned-on-glass photolithographic mask (Microtronics) having our desired anode geometry. The mask was exposed to ultra-violet light (365 nm, 8 mW/cm²) for 12 s and transmitted the radiation through its clear fields onto the portions of the resist to be washed away. The cell was submerged in a developer (Microposit CD-30, Rohm and Haas) for 3 min to wash away the exposed resist. Then the cell was hard baked in an oven at 120 °C for 6 hrs before the excess Ni was etched away. A nitric acid based nickel etch (Type TFB, Transene Company, Inc.) was poured into a beaker and heated on a hot plate to 55 °C. The cell was submerged in the acid for typically 2 min until the excess nickel was completely etched away. The remaining photoresist was then removed by rinsing the pattern in acetone, ethanol, methanol, and water. The time periods for which the cell was exposed to UV light, submerged in the developer and in the acid

bath were optimized to closely mimic the photolithographic mask geometry and prevent significant over-etching or under-etching.

The continuity of the nickel patterns were visually examined before electrochemical testing using a digital camera (CoolPix 990, Nikon) mounted on an optical microscope (Optiphot, Nikon). The electrical continuity of the patterns was not checked using such tools as multimeter probes in order to avoid scratching the patterns. An SEM (Amray 1820D) was used to resolve the fine structure of the TPB lengths of the Ni/YSZ interface along the pattern edges. To reduce charging effects SEM samples were coated in a solution of 60 % Au/40 % Pd (15 nm) via thermal evaporation before being exposed to a 30 keV electron beam to resolve the images. This process was destructive to the samples and thus only done for so many anodes in order to provide necessary pre-experiment structural characterization. The SEM micrographs of pattern edges after anode microfabrication, which were jagged and rough due to the acid etching procedure, were visually processed to estimate actual TPB lengths. A section of TPB (geometrically $10.00\text{ }\mu\text{m}$ ($\pm 0.08\text{ }\mu\text{m}$) long, much longer than the scale of the TPB roughness features) from 5 different patterns were approximated by a series of straight line segments each $0.50\text{ }\mu\text{m}$ ($\pm 0.08\text{ }\mu\text{m}$) long. The end points of the line segments resided on the TPB and the summed length of these segments were used to approximate the actual TPB length. Accuracy in estimating the TPB shape could have been gained by reducing the lengths of the approximating segments but this was avoided due to the associated increase in the compounded uncertainty.

A profilometer (Alpha-Step 500 Surface Profilometer, Tencor Instruments) was used to measure the change in vertical thickness of the anode patterns and to perform “scratch tests” to assess the adherence of the anodes to the YSZ. The profile scans used a stylus translating at 200 $\mu\text{m/s}$ while applying 10.1 mg force normal to the surfaces. The stylus tip of the profilometer was positioned on the YSZ within 100 μm of the interrogated nickel anode and then swept over the anode for a total scan length of 1 mm recording the vertical displacement of the stylus at 50 Hz.

For the results in this thesis study, the mask used in the photolithography process was designed to produce four electronically independent Ni patterns and two electronically independent Ni reference electrodes as shown in Figure 2.1. Although other pattern arrangements with varying TPB lengths were also tested for kinetic measurements, results from those tests are not reported here. Electrochemical results from the other patterned anode configurations that have been fabricated are reported elsewhere.³⁰ Each patterned anode consisted of a group of 10 parallel Ni “strips” (of equal width) connected at the ends by 20 μm wide Ni “current collector bars”. The width of the strips was different for each pattern and so they are referred to by the width of their strips, e.g. the 25 μm pattern is the pattern with 10 parallel Ni strips each 25 μm wide. All patterns were contained within a 2 mm by 3 mm rectangle and the centerlines of the strips for each pattern were separated by approximately 221 μm . The two Ni reference electrodes were 20 μm wide and terminated at a point equidistant to the two closest patterns (approximately 2 mm from them). The reference electrodes did not function as well as anticipated and future improvements

to the patterns would involve creating point references to avoid changes in potential over the distance of the reference electrodes that reduced their effectiveness in this study.

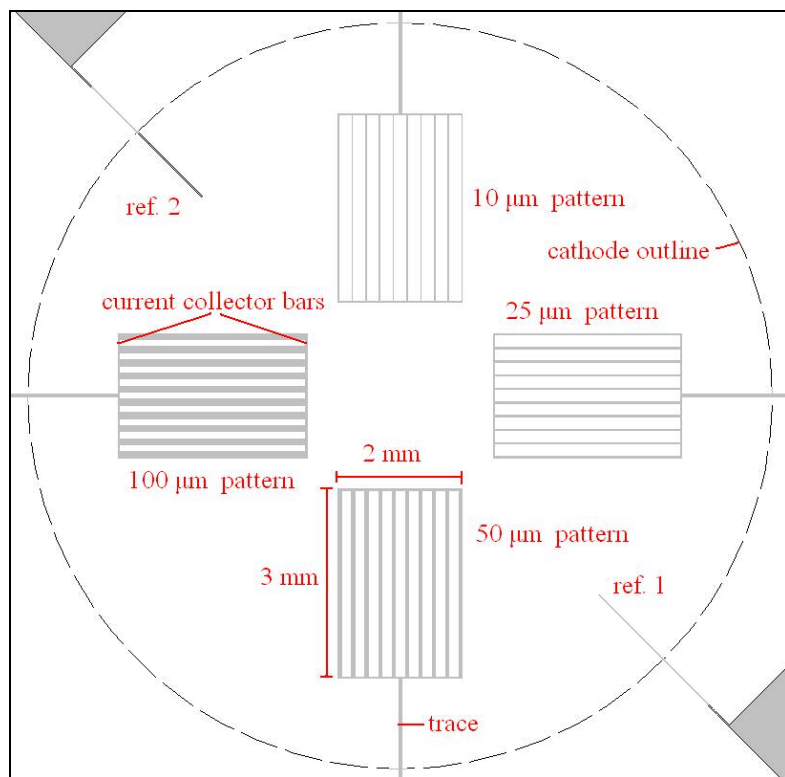


Figure 2.1: Schematic of the four patterned Ni anodes, two Ni reference electrodes and outline of the cathode.

Each of the reference electrodes and the four anodes had one Ni “trace” (50 μm wide) that extended 0.5 mm past the outline of the cathode where it connected to a large Ni pad that resided at one of the four corners of the electrolyte as shown in Figure 2.2. The traces were made relatively thin so that they would not contribute much to the electrochemistry of the Ni patterns.

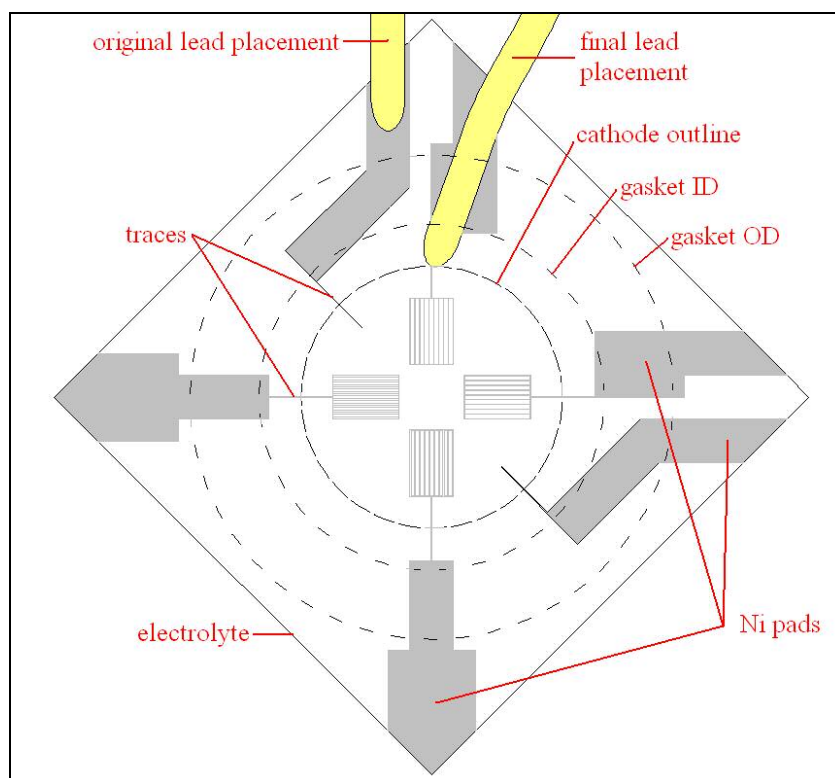


Figure 2.2: Schematic of photolithographic mask design detailing patterned Ni anodes, traces and Ni pads. Outline of cathode as well as outline of sealing gaskets shown as dotted lines; example anode lead placements are also shown.

Originally, the anode chamber was to be sealed from the outside atmosphere by pressing circular gaskets against the electrolyte and the current collecting Ni pads. Under such a configuration, the external electronic conductors, or leads, were attached to the Ni pads at the corners of the electrolyte outside of this anode chamber as shown in Figure 2.2. Therefore, the pads were made relatively wide to 1) reduce the possibility that scratches from the gaskets would break the electron conduction path from pattern to lead and 2) to increase the ease in which the leads could be attached to the pads. However, attaching the leads to the Ni pads at the corners of the

electrolyte often resulted in a broken electron conduction path due to interactions between the Ni pads and the gasket material. So instead the leads were brought to the inside of the anode chamber and attached to the Ni trace/pad intersection.

The entire anode side design of a typical MEA used in this study is shown in Figure 2.3. Note that the circular cathode on the opposite side of the electrolyte can be seen through the translucent (single crystal) electrolyte. Only five of the many MEA's fabricated are reported here and they are numbered (MEA 1, MEA 2...) with respect to the order in which they were electrochemically tested.

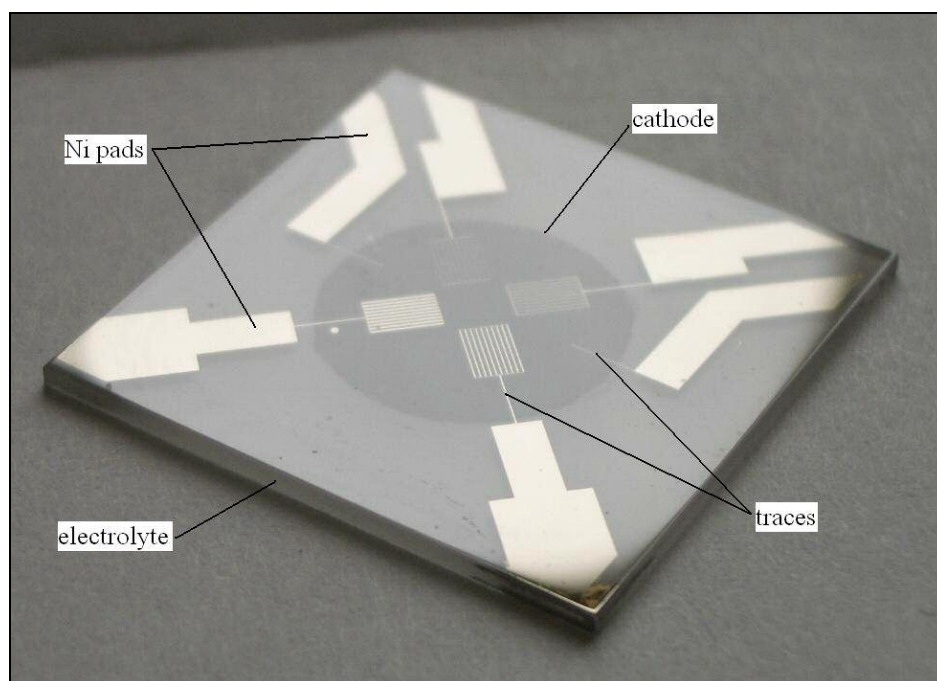


Figure 2.3: Representative MEA detailing the four Ni patterns and two Ni reference electrodes (dark circle seen in the center of the translucent electrolyte is the cathode which resides on the far side of the electrolyte).

Each anode pattern had approximately the same length of TPB with negligible differences arising due to the variation of TPB length of the inside of the current collector bars. The area of the cathode assumed to be in ionic communication with each anode was taken as the 2 mm by 3 mm area that bounded each anode plus an additional border region around the perimeter of this rectangular area that was one electrolyte thickness wide. The experimental data for impedance measurements is normalized to these areas, which for the 1 mm thick electrolytes is 0.2125 cm^2 and for the 0.5 mm thick electrolytes is 0.1350 cm^2 . Other relevant geometric parameters of the four patterned anodes are given in Table 2.2.

Table 2.2: Geometric parameters of the four patterned Ni anodes. The section of the trace that is within the outline of the cathode is included in the calculation of l_{TPB} , and

$$A_{Ni}.$$

Pattern strip width (μm)	10	25	50	100
l_{TPB} , length of TPB (m)	0.0707	0.0704	0.0699	0.0689
A_{Ni} , Ni/YSZ contact area (cm^2)	0.00453	0.00903	0.0165	0.0315
YSZ space between strips (μm)	211	194	167	111

Two thin reference electrodes (far from the patterns) were intended to serve as voltage references for the overpotentials applied to each anode. This way the current that each anode drew could be associated with its change in potential referenced to an inactive area of electrolyte surface. In other words only the so-called anodic overpotential would be measured as a function of current through the cell and not the overpotentials associated with ionic transport through the electrolyte and activation of the cathode. Reference electrode 1 was to be used in conjunction with the 25 μm and

50 μm patterns and reference electrode 2 in conjunction with the 10 μm and 100 μm patterns. In these configurations, the reference electrodes would be more than three electrolyte thicknesses away from the anodes they were polarizing, ensuring that the change in electrolyte surface potential near the anode due to the flow of current would not affect the potential of the reference electrode.³¹ However, during experimental testing it was found that the differences in OCV between the reference electrodes and their associated anodes were too large to warrant using them as proper reference electrodes and so the cathode was used as a reference electrode. It is likely that changes in the electrolyte potential along the length of the reference electrodes caused this difficulty, which could be avoided in the future by using a point contact reference electrode.

2.2 Experimental Setup

2.2.1 MEA Wiring

The external leads for the electrodes were each constructed of gold wire (Alfa Aesar, 99.9 % metals basis), 10 cm long and 0.25 mm in diameter twisted to a silver wire 25 cm long. In general 5 leads were made, one for the cathode and 4 for the four patterned anodes (two leads for the two reference electrodes were made for MEA 1). The wires were insulated using small diameter ceramic tubes (Ceramic TC Insulators, Omega Engineering, Inc.) inside the furnace and PTFE tubing outside of the high temperature regions.

As previously mentioned to increase the success of achieving a continuous electron conduction path from pattern to external leads the wires were connected to the Ni traces inside the anode chamber shown in Figure 2.2. To do this without causing appreciable leaks through gaps between sealing gaskets and electrolyte, the ends of the gold wires (9 mm) were left un-insulated and were flattened to 0.05 mm. The procedure for attaching the external leads to the four patterned anodes is given in the following. First, the end of the flattened gold wire was fixed to the nickel trace using a needle point while the un-flattened part was fixed to the closest corner of the electrolyte using a zirconia based ceramic paste (Ultra-Temp 516, Aremco Products, Inc.). After the ceramic paste was dried in air the underside of the flattened gold wire tip was coated in gold ink, fixed on the nickel trace using the same needle tip and dried under a heat gun ($60\text{ }^{\circ}\text{C} \pm 5\text{ }^{\circ}\text{C}$) for 2 hrs. Figure 2.4 shows a detail of the needle tip fixing a gold lead to the trace of a reference electrode of MEA 1 along with the other pattern leads attached to the electrolyte via ceramic paste. After all the leads bonded to the Ni trace via dried gold ink, ceramic paste was applied over the lead tips to hold them securely in place. Next, circular layers of glass (Borosilicate glass filter, Cole-Parmer Instrument Company) and mica (muscovite mica, McMaster Carr) gaskets were attached to the anode side of the electrolyte using the same high temperature ceramic paste. They were fixed using the ceramic paste so that the gaskets would not shift out of place during loading of the MEA into the experimental rig. All gaskets had an ID = 15.9 mm, and an OD = 25.4 mm. Two layers of the glass gasket were placed against the electrolyte followed by one layer of mica followed by two more layers of glass.

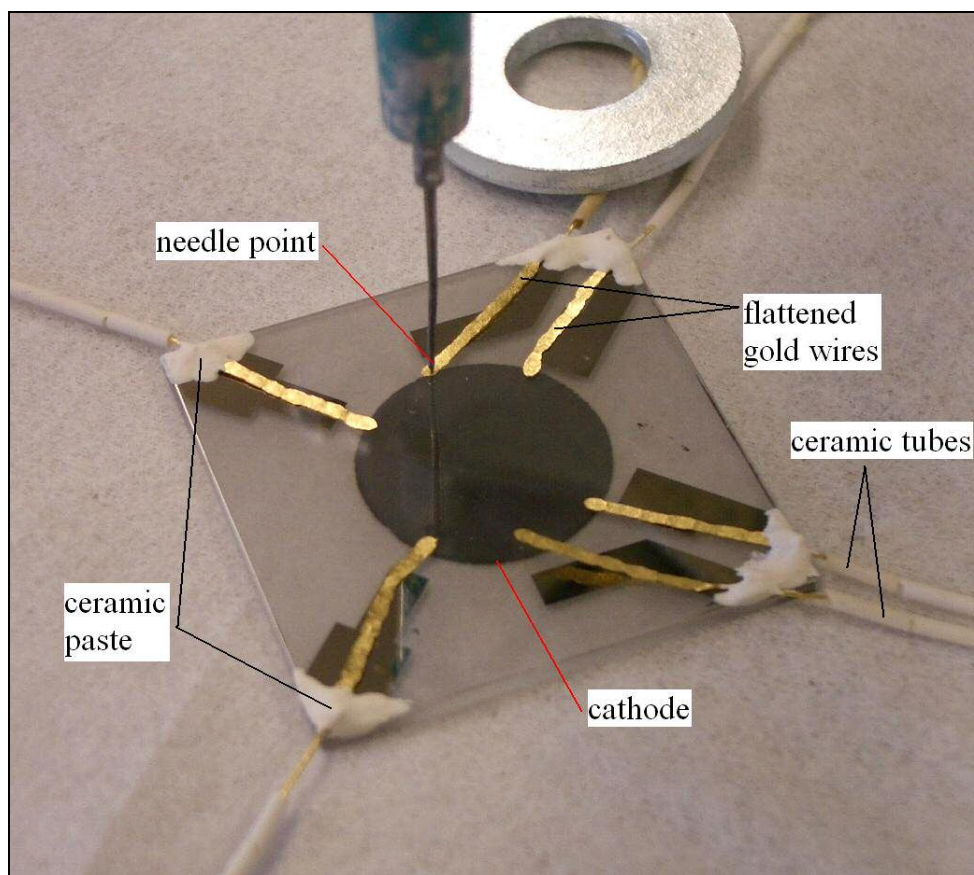


Figure 2.4: Anode side of MEA 1 detailing a flattened gold lead fixed to a reference electrode via needle tip as well as the attachment of the other pattern's gold leads to the electrolyte via ceramic paste.

The glass gaskets served two functions. Firstly, at the high working temperatures, the glass melted and filled in gaps between the electrolyte/mica and mica/experimental rig interfaces thereby hermetically separating the anode chamber from the surrounding atmosphere. Secondly, the soft glass at high temperature allowed the electrolyte to expand relative to the experimental rig during heat up and cool down to eliminate thermal stresses that would otherwise cause fracture. The mica gasket prevented the soft glass from fusing the electrolyte and experimental rig together as

it solidified together during cool down so that the electrolyte could be easily removed from the experimental rig for post electrochemical testing analysis. Figure 2.5 shows the anode side of a typical MEA with all leads and gaskets attached via ceramic paste.

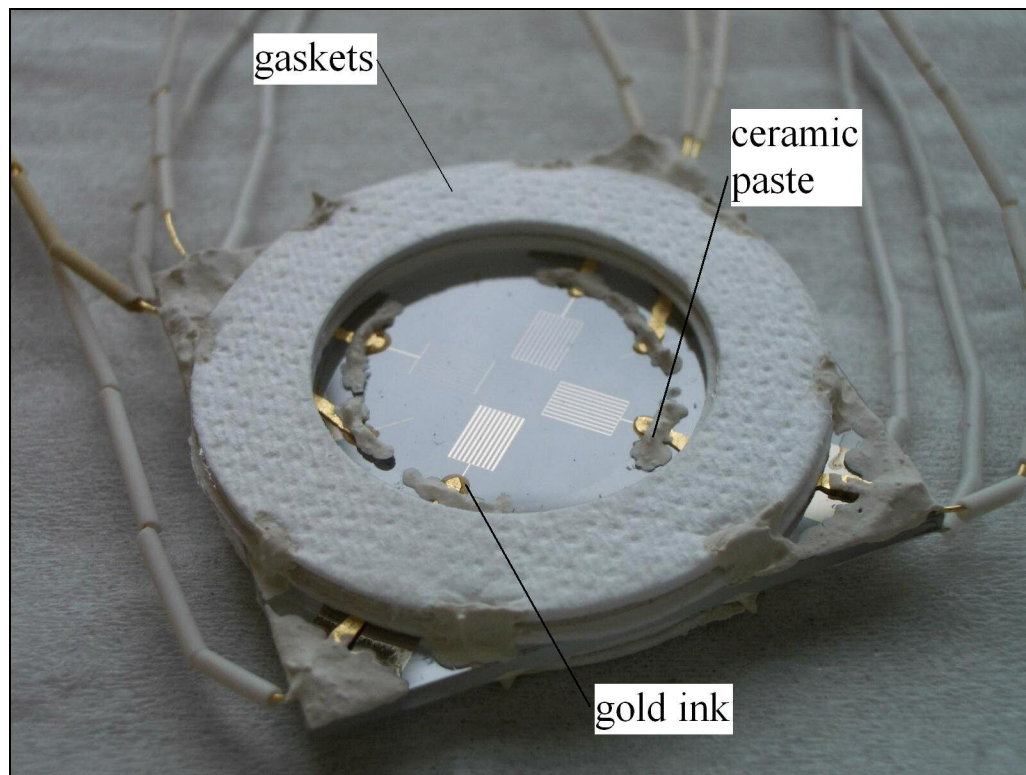


Figure 2.5: Anode side of typical MEA showing all leads and gaskets attached via ceramic paste.

The cathode lead was then fixed to the cathode in the manner described above. In addition a grid of gold paste was painted over top the cathode to provide a uniform and sufficient supply of electrons to the cathode. Although a large fraction of the cathode was covered by the gold paste, excess flow of O_2 was provided to minimize its contribution to overpotentials. In addition, experimental data on LSM/YSZ/LSM symmetric cells indicate that cathode overpotentials contribute less than 10 % to total

cell overpotentials. Two unshielded k-type thermocouples (0.01” diameter, Omega Engineering Inc.), TC1 and TC2, were also pasted to the cathode side of the MEA. TC1 was used as the feedback thermocouple in the furnace controller to modulate the electrolyte temperature. The same gasket arrangement was fixed to the cathode side of the disk using ceramic paste. Figure 2.6 details a wired cathode with attached thermocouples.

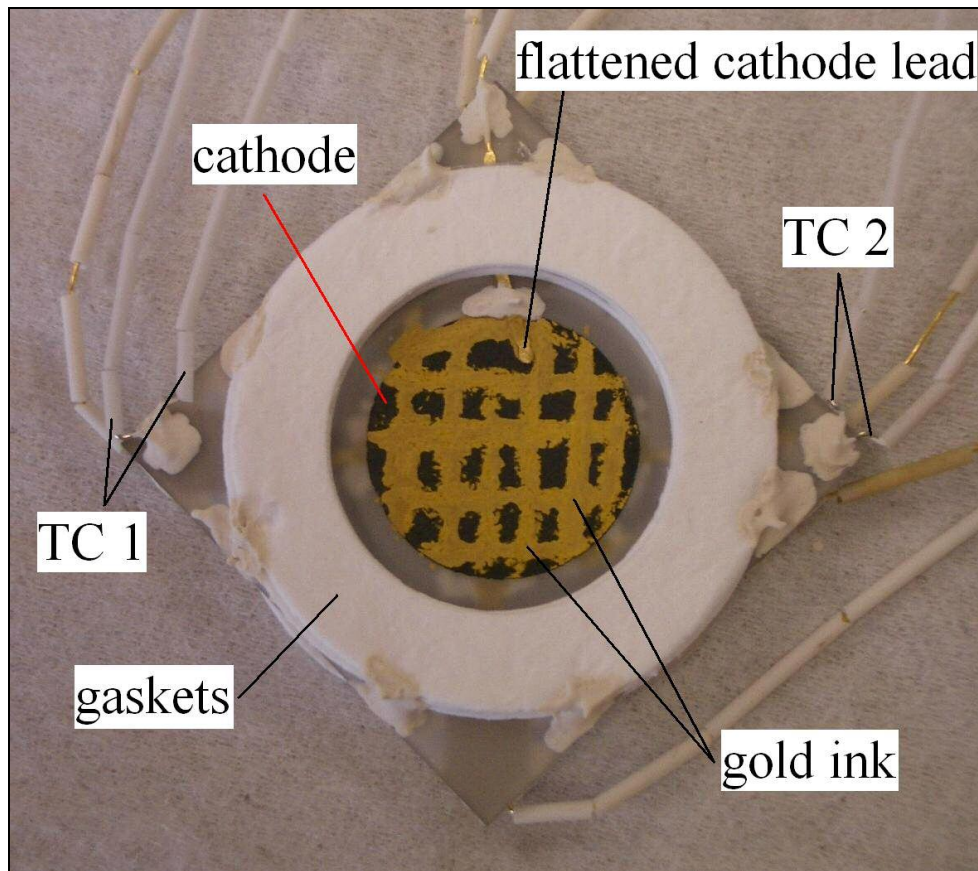


Figure 2.6: Cathode side of MEA detailing cathode lead attachment, gold ink electron supply grid, gaskets, and thermocouples.

2.2.2 Experimental Rig

The wired MEA was placed between two fully dense cast alumina tubes (AC Technologies, Inc.). The alumina tubes were supported by a furnace and “compression rig” that were fixed in space by a simple home made stand. The furnace rested on black straps that spanned across the stand’s two horizontal aluminum bars. The horizontal steel bars of the compression just above the stand’s aluminum bars were fixed to the stand’s vertical aluminum bars. Figure 2.7 shows an overall picture of the experimental setup.

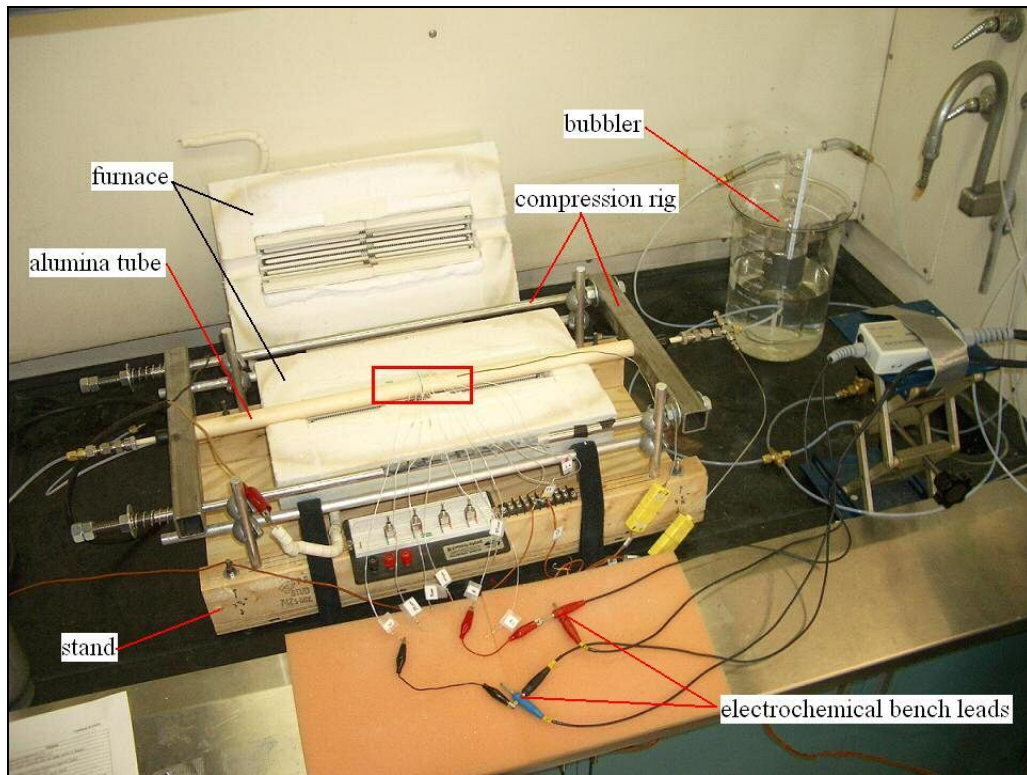


Figure 2.7: Experimental setup showing home made stand, furnace and compression rig, the red square inset is blown up in Figure 2.8.

Figure 2.8 shows the inset of Figure 2.7 and details a loaded MEA.

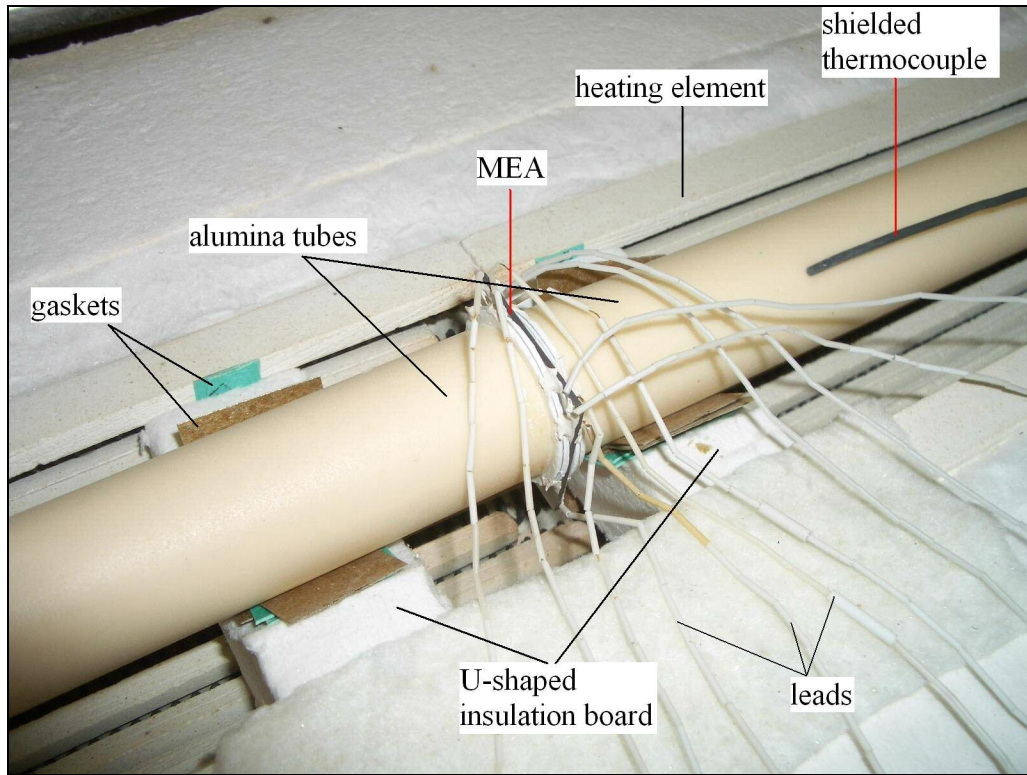


Figure 2.8: Inset from Figure 2.7 showing a detail of a loaded MEA and alumina tubes supported by the furnace.

Blocks of insulation board were cut to into “U” shapes and placed on the heating elements of the furnace to keep the alumina tubes fixed in space as shown in Figure 2.8. Sheets of high temperature gasket were used as shims to fine tune the alignment of the alumina tubes.

A designed compression rig was critical to avoiding unwanted YSZ electrolyte cracking in the experiments; the compression rig oriented the alumina tubes horizontally in space, applied pressure to the electrolyte necessary for sealing and

prevented transference of thermally induced stresses to the electrolyte during temperature cycling. Figure 2.9 shows a schematic of the compression rig.

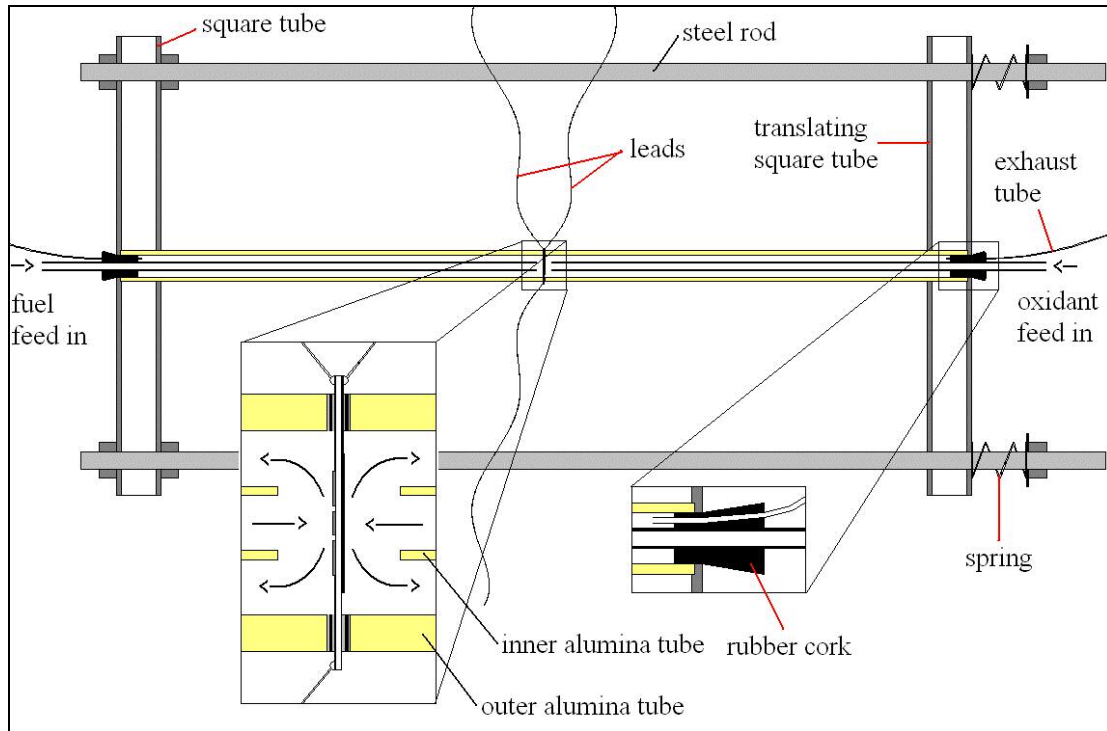


Figure 2.9: Schematic of compression rig with inset of loaded MEA and rubber cork end cap.

Each of the two outer alumina tubes was set in one of the two square steel tubes shown in the far right and far left of Figure 2.9 (the alumina tubes are perpendicular to the square tubes but are in the same plane). The square tube on the far left of Figure 2.9 was fixed to the horizontal steel rods, whereas the square tube on the far right of Figure 2.9 was allowed to translate along these horizontal steel rods. Compression springs were fixed to the horizontal steel rods and pushed the translating square tube and embedded alumina tube toward the opposing alumina tube. The

MEA and gasket assembly was compressed between these two outer alumina tubes; a compressive force of 9 N distributed over the tube/gasket interface (~ 47 kPa) prevented leakage of reactant gases and fracture of MEA's. As the alumina tubes expanded during heat up the square tube translated such that the external springs were additionally compressed thereby preventing excessive loading of the MEA and subsequent fracture as observed in many previous experiments.

Each outer alumina tube had an OD = 22.2 mm and an ID = 15.9 mm and was 30.5 cm long. Outside the furnace the ends of the outer tubes were sealed from the atmosphere using a rubber cork. An inner alumina tube (OD = 6.3 mm, ID = 4.8 mm, length = 35.5 cm) was positioned inside the outer tube to deliver the fuel feed to the anode and the oxidant feed to the cathode. The inner tubes were passed through a hole in each rubber cork such that the tube ends were positioned 5 mm away from their respective electrodes. This geometry created an impinging jet flow. By flowing substantial excess fuel and oxidant in the anode and cathode chambers respectively, species consumption did not result in significant species gradients over the surface of the anode and cathode. The electrode chamber exhaust gases traveled through the annular passage between the inner and outer ceramic tubes before passing to the atmosphere via a 3.1 mm diameter PTFE tube that passed through each rubber cork as shown in the inset in Figure 2.9.

2.2.3 Temperature and Flow Control

This assembly was placed in a tubular resistive furnace (High Temperature Electric Heater, Fibercraft) with 15 cm of both the fuel feed tubes and oxygen feed tubes inside the furnace during testing. The remaining 15 cm of each tube were outside the furnace and cool enough to use the rubber cork and rubber O-ring contained in the Swagelok vacuum seal fitting to seal the anode and cathode chambers from the surrounding atmosphere. The temperature of the furnace was controlled using a programmable temperature controller (Athena Temperature Controller, Allied Electronics, Inc.). The thermocouple (TC1) attached to the cathode side of the MEA was used as the feedback signal for this controller so that the temperature of the MEA could be directly controlled. The other thermocouple attached to the MEA (TC2) along with two shielded thermocouples were connected to a terminal block fixed near the furnace. TC2 and the shielded thermocouple shown in Figure 2.8 were used to check that the control TC1 was working properly and as a safety measure to check for fuel leaks. The other shielded thermocouple was positioned in the anode side flow outside the furnace and used to measure the humidified fuel feed inlet temperature. Preliminary experiments showed that varying the amount of the fuel and oxidant flows did not influence the temperature of the MEA, i.e. both fuel and oxidant flow reached the electrolyte temperature before impinging on the MEA for flow rates greater than those used in the experiments.

The experimental gases were directed from compressed bottles through PTFE tubing to five mass flow controllers (MFCs) (5850E Thermal Mass Flow Controller, Brooks

Instrument). Three MFCs regulated the flow of fuels and argon to the anode and two others regulated the flow of oxygen and argon to the cathode. For the experiments using humidified fuel feeds, the fuel flow was directed through a water bubbler. The bubbler and a mercury thermometer were partially submerged in a beaker of water that maintained a temperature of 25 °C during all experiments.

The signals to and from the mass flow controllers and thermocouples were handled by two data acquisition boards (SCXI 1102 Thermocouple Amplifier, National Instruments) (PCI-6034 multifunction I/O board, National Instruments). Labview software run from a desktop PC was used to control the MFCs and read the MFC and thermocouple outputs. In this program the user specified the flow rate of fuel to the anode and the other flows were directed to be a multiple of this flow, i.e. the anode diluent was two times the fuel flow, the oxidant was 5 times the fuel flow and the cathode diluent was 2.5 times the fuel flow. The electrochemical data was collected by an electrochemical bench (Autolab PGSTAT 30, Eco Chemie) as described in the following section.

2.3 Electrochemical Measurements

Two different wiring configurations were used to record electrochemical data: the 3-probe configuration and the 2-probe configuration both are shown in Figure 2.10.

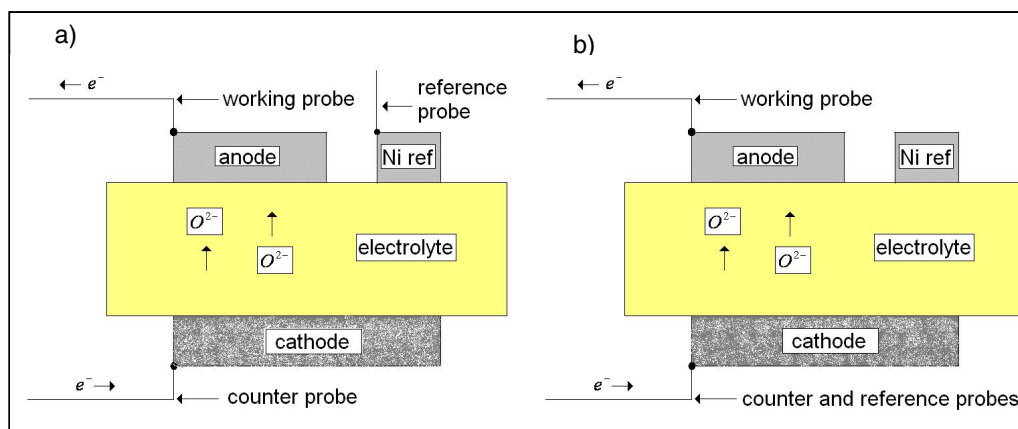


Figure 2.10: MEA wiring configurations a) 3-probe, b) 2-probe.

The electrochemical bench can control and measure both voltage and current. For this study the electrochemical bench was set to potentiostatic mode, meaning that the voltage, or overpotential, was the user specified input and current the output. The overpotential was applied between the working probe and the reference probe and the current measured was that current flowing from counter probe to working probe through the external leads.

In the 3-probe configuration the reference probe was connected to the Ni reference electrode, whereas in the 2-probe configuration the reference probe was shorted to the counter probe and connected to the cathode. The 3-probe configuration takes advantage of the Ni reference electrode in that only the overpotential associated with activation and ohmic losses in the anode should be measured as a function of the anodic current. Thus, the anodic overpotentials as a function of current are directly measured, if the electrolyte potential at the anode and the reference are equal. The 3-probe configuration was used for MEA 1 but as mentioned in section 2.1.2 it was

found that the references did not behave as desired (the difference in OCV between the Ni references and the pattern anodes was over 100 mV) and so the 2-probe configuration for used for the remainder of the experiments.

The two different electrochemical measurements taken were sweep voltammetry ($V-i$) and electrochemical impedance spectroscopy (EIS). In sweep voltammetry, the user specifies the starting and ending voltages (overpotentials) to be applied between the working and reference probes. The potentiostat steps through this voltage range recording the current flowing from working the counter probe at each voltage. The result is usually plotted as a $V-i$ curve with cell voltage on the abscissa and cell current density of the ordinate. For the tests utilizing CO and CH₄ as the fuel, the Ni pattern's OCV's were low and so the voltage sweeps were kept low so as to avoid Ni oxidation (thermodynamic limit of NiO reported to occur at 0.72 V at 775 °C).³² For the plots presented here the ohmic losses for each MEA were subtracted from the $V-i$ plots to normalize the data relative to the different thicknesses (i.e. different ohmic contributions) of each MEA.

In the EIS measurements, a small amplitude ac voltage signal is applied on top of a constant dc voltage signal. The current response is a sinusoidal signal and the voltage input can be divided by the current output to yield and impedance with a real and imaginary part. The frequency (ω) of the input voltage signal is varied across a spectrum of frequencies, from high to low, and the real component of impedance is plotted on the ordinate and the negative of the imaginary component of the

impedance is plotted on the abscissa. An example of an EIS plot is shown in Figure 2.11.

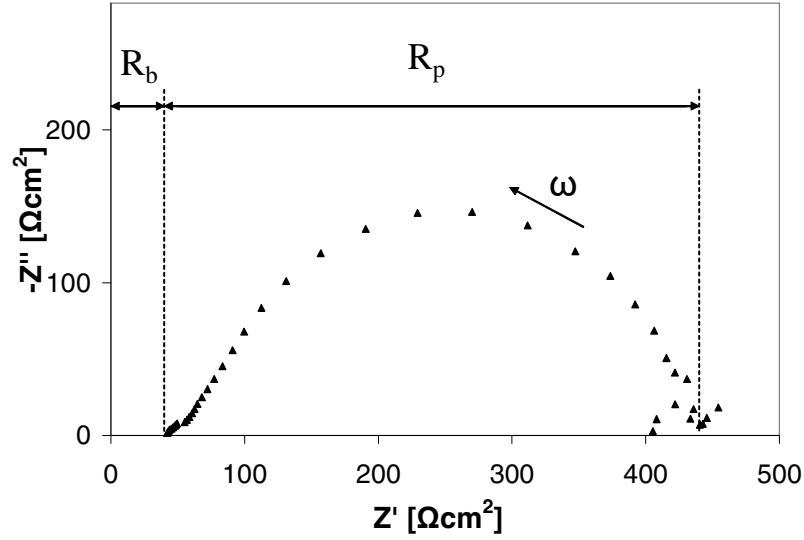


Figure 2.11: Sample EIS plot showing area-specific impedance with excitation frequency (ω) increasing from right to left as shown. Area-specific bulk resistance (R_b) and polarization resistance (R_p) are also indication in the plot.

Each point on the curve has a real impedance component (Z') and an imaginary impedance component (Z''). The imaginary component arises due to the shift in phase between the input voltage signal and the output current signal and arises from capacitive effects associated with charge transfer and diffusion of species along the surface. Purely resistive behavior of the fuel cell is usually captured at the high frequency end (far left on plot) and low frequency end (far right on plot). Usually at the highest frequency capacitive effects disappear and the plot intercepts the real axis. This intercept is termed the bulk resistance (R_b) and it represents the electrolyte's

resistance to ion transport. At the lowest frequency (\sim dc signal) the plot again intersects the real axis and this intercept is called the total cell resistance. The difference between this intercept and R_b is termed the polarization resistance (R_p) and is associated with the losses in both electrodes. The total cell resistance (obtained by an EIS measurement conducted with a 0 V dc superimposed signal) minus the bulk resistance and resistance associated with the other electrode is termed the charge transfer resistance (R_{CT}) and is the portion of R_p associated with one electrode. R_{CT} is directly proportional to the slope of the V - i curve of the same cell at $i = 0$ after R_b and the resistance associated with the other electrode have been subtracted. The range of frequencies of the EIS measurements in this experiment was from 100 kHz to 300 mHz with an ac voltage signal amplitude of 10 mV. The low frequency data in some of the EIS plots have appreciable imaginary components because the lowest frequency used to interrogate the MEAs was relatively large in order to speed up the data taking process.

2.4 Range of Conditions Studied

Many MEA's were tested in this study, but only a small portion of them are reported herein; two (MEA's 1 and 2) operated on humidified H_2 , two (MEA's 3 and 4) on humidified CH_4 and one (MEA 5) on humidified CO. These three fuels provided a basis for understanding the behavior of the patterned anodes operating on fuel species expected to occur when pre-reforming reactions are used to convert heavier hydrocarbon fuels upstream of the anode. Hydrogen tests were conducted to provide a baseline to compare results from future tests on other fuels including CO and

hydrocarbons. The performance of the polarized electrode for the carbon containing fuels, CO and CH₄, was expected to degrade, if at all, more slowly than those anodes kept at open circuit conditions due to the oxygen ion flux to the polarized anodes which can likely reduce carbon deposition via electrochemical oxidation.

But before any electrochemical testing was done the effect of a high temperature reducing environment on the patterned anodes was studied. MEA 2 was heated to 800 °C in a 5 % H₂ / 95 % Ar atmosphere for 4 hours (no electrochemistry or associated O²⁻ flux) to examine this effect. MEA 2 was wired up and fixed in the compression rig for electrochemical testing after the electrochemical testing of MEA 1. All MEA's were heated to and cooled from the appropriate working temperature at a rate of 1 °C per min. During this time, the MEA's were exposed to reduced flow rates of dry fuel and oxidizer. Once the working temperature was reached all the MEA's were exposed to a flow of dry H₂ and Ar (anode side) and O₂ and Ar (cathode side) and preliminary electrochemical data was taken to examine there initial performance. Then the humidified primary fuel flows were introduced and the electrochemical experiments began. The experiments consisting of a heat up, initial testing, cool down and main "phase"; the experimental conditions of these phases are given in Table 2.3. Note: during the cool down phase for the CO and CH₄ experiments only Ar was flown on the anode side to avoid uncontrolled carbon deposition and hopefully sustain only deposits on the Ni or anode-side YSZ that occurred at the high-temperature test conditions. For MEA 1 EIS data was recorded for all the patterns at 700 °C, 750 °C and 800 °C to see if high temperatures would


































cause the patterns to peel off or otherwise behave poorly. The total cell resistance of MEA 1 did not increase drastically for temperatures up to 800 °C as has been observed in previous experiments on different MEA's and so the electrochemical testing was carried out at this temperature. MEA's 2 – 4 were tested at 750 °C to balance the effects of lower ohmic resistance at high temperatures and lower total cell resistances at lower temperatures. EIS measurements were taken for the anodes for all MEA's until steady state operation was reached. Then an overpotential was applied to one of the anodes for 2 hrs and is referred to as a period of polarization. Although future tests will have four different potentials on each electrode, existing test facilities did not permit such tests for the current study. The overpotential on the selected pattern was removed after 2 hr and EIS and sweep voltammetry measurements were recorded for all anodes. These intermittent measurements took approximately 40 min and are referred to as periods of open circuit conditions. The periods of open circuit conditions followed by periods of polarization are termed experimental periods and these were repeated for each MEA until the entire experiment was terminated. Table 2.4 lists the parameters of each experimental periods as well as the experimental timeline for each MEA. The timelines in Table 2.4 consist of thin and thick bars. The thin bars cover the times in which all anodes were under open circuit conditions and the thick bars cover the times at which the listed pattern was polarized with the listed overpotential.

Table 2.3: Experimental conditions for the various phases of the experiments reported in this study.

Experimental Phase	MEA	Temperature [°C]	Anode Side				Cathode side		
			Fuel (sccm)	H ₂ O/H ₂	Diluent (sccm)	Velocity [cm/s]*	Oxidant (sccm)	Diluent (sccm)	Velocity [cm/s]*
Heat up	1 - 5	25	H2 (10)	-	Ar (100)	35	O2 (50)	Ar (25)	24
Initial testing	1 - 5	750	H2 (100)	-	Ar (200)	96	O2 (500)	Ar (250)	240
Main	1	800	H2 (100)	0.05	Ar (200)	96	O2 (500)	Ar (250)	240
Main	2	750	H2 (100)	0.05	Ar (200)	96	O2 (500)	Ar (250)	240
Main	3	750	CH4 (100)	0.05	Ar (200)	96	O2 (500)	Ar (250)	240
Main	4	750	CH4 (100)	0.05	Ar (200)	96	O2 (500)	Ar (250)	240
Main	5	750	CO (100)	0.05	Ar (200)	96	O2 (500)	Ar (250)	240
Cool down	1 - 2	25	H2 (10)	-	Ar (100)	35	O2 (50)	Ar (25)	24
Cool down	3 - 5	25	-	-	Ar (100)	32	O2 (50)	Ar (25)	24

* Inner tube velocity at calculated assuming ideal gas law (at 750 °C)

Table 2.4: Parameters of the experimental periods and experimental timeline for each MEA reported in this study.

MEA	Pattern (μm)	η (mV)	0 hr	2 hr	4 hr	6 hr	8 hr	10 hr	12 hr	14 hr
1	100	600								
2	50	200								
3	50	100								
4	25	80								
5	100	200								
Key:			open circuit		polarized		experimental period			

After electrochemical tests were completed the patterned anodes and YSZ surfaces were probed using Raman (with a Renishaw In-Via Raman Microscope), energy dispersive X-ray analysis (EDAX with a Amray 1820D), and X-ray diffraction analysis (XRD with a Bruker C2 Discover X-Ray Powder Diffractometer). The Raman measurements consisted of irradiating the sample with two monochromatic sources (15 mW, argon ion $\lambda = 433$ and helium/neon $\lambda = 633$ nm) and collecting the scattered light to look for Raman-shifted signals and thereby derive species composition data for the surface and near surface. A good reference describing Raman spectroscopy for surface species is given and will not be discussed here.³³ The Raman spectra are presented as intensity versus Raman shift in wavenumbers [cm^{-1}] to identify the dominant surface and near-surface species. The intensity peaks were then matched with reference material³⁴ to determine the species present on the surface of the sample.

For the EDAX measurements an X-ray beam (20 keV accelerating voltage) struck the sample and the X-rays emitted by the sample were absorbed by a collector to determine the elements present within the sampling region.³⁵ Similarly in the XRD analysis a CuK_α radiation source was emitted on the sample at a 2-theta scan range from 4° to 90° and a HiStar area detector gathered the diffracted X-rays. A MDI Jade software package was used to identify the compounds detected in the sample.

These measurements were conducted on the Ni and YSZ surfaces of the MEA's operating on CO and CH_4 after the electrochemical experiments were completed. The results of the measurements indicated which species were likely to be present on and near the Ni and YSZ surfaces during the electrochemical tests and were used to build theories explaining the electrochemical behavior of the polarized Ni patterns.

Chapter 3: Non-electrochemical Test Results

The sputter deposition method of coating the YSZ with nickel was expected to produce dense nickel coatings that adhered well to the YSZ surface. The photolithography process was used to create quantifiable lengths of TPB in four electronically independent microfabricated patterned anodes. The anode patterns used in this study all had similar geometric TPB's of approximately 0.07 m (Table 2.2). Since it is often assumed that reaction rates scale with TPB^{2, 28} similar performance was expected for these four equal-TPB length patterns.

The high temperatures at which the experiments were conducted lead to Ni grain growth and smoothening of the TPB as seen in previous studies.¹ The Ni roughness features along the TPB created by the acid etching agglomerated into large Ni grains that increased the length scales associated with the TPB roughness and thereby reduced the actual TPB length. The tests reported in this chapter detail how the patterned anodes reveal significant differences when exposed to different anode overpotentials.

The microfabrication process produced high quality patterns, i.e. the patterns followed the geometry of the photolithography mask and were free of significant discontinuities, holes and cracks. Figure 3.1 shows the anode side of MEA 2 after anode wiring and heat treatment (800 °C in a reducing atmosphere without electrochemistry as describe in section 2.4). Figure 3.1 also serves as a map

indicating the location of the highly magnified pictures presented in the remainder of this thesis. The gold lead attachments for the two nickel reference electrodes and the ceramic paste around the boundary of the patterns can also be seen in Figure 3.1. The patterned anodes – identified as, clockwise from the top: 10 μm , 25 μm , 50 μm and 100 μm patterns – are deposited on the translucent single crystal electrolyte. The dark LSM/YSZ cathode is seen through the electrolyte as well as shadows of the anode patterns projected onto the cathode/electrolyte interface.

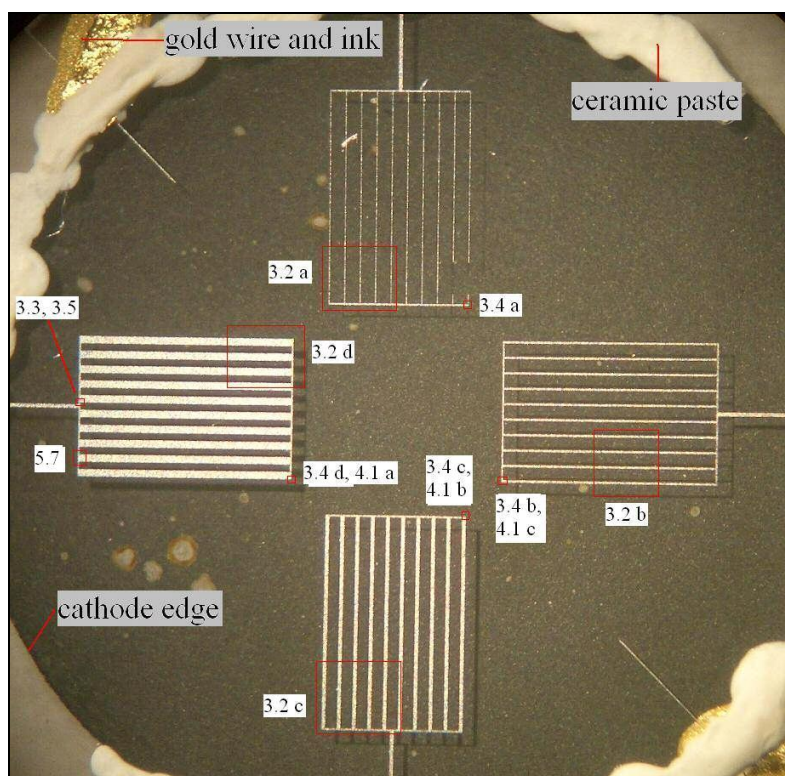


Figure 3.1: Optical microscope picture (10X magnification) of MEA 2 after heat treatment; the digitally added red boxes show areas photographed for figures presented in this study as numbered.

The quality of the patterned anodes produced via sputtering and photolithography are illustrated in Figure 3.2. The pictures in Figure 3.2 are representative of all the patterns tested. Visual examination of these pictures (60X magnification) suggests that the patterns are continuous and free of cracks or pores down to the resolution of the optical image ($< 5 \mu\text{m}$).

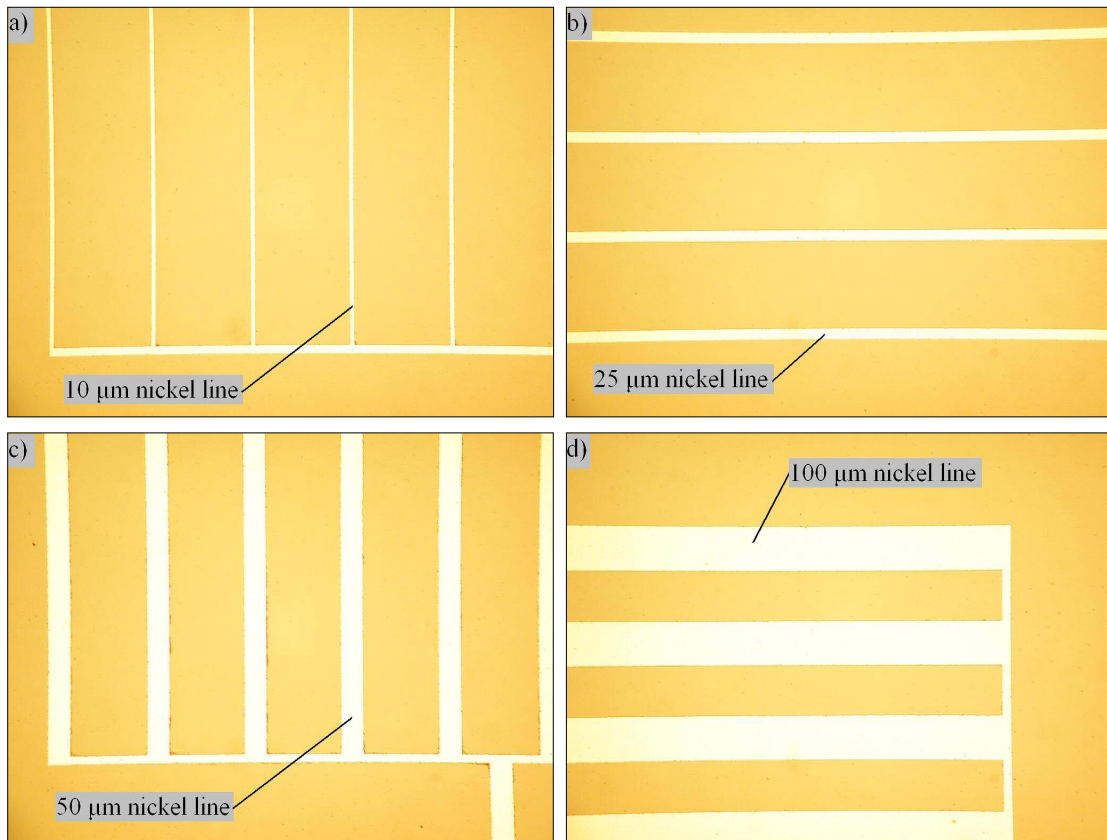


Figure 3.2: Optical microscope pictures (60X magnification) of the anodes from MEA 1 taken after anode fabrication: a) 10 μm anode, b) 25 μm anode, c) 50 μm anode and d) 100 μm anode.

A total of three localized pattern defects for the five MEA's tested that resulted in Ni line discontinuity and/or failure to reproduce the exact mask geometry were detected

when examining the MEA's under the optical microscope. These defects are described further in Appendix A. To estimate the loss of Ni area and TPB resulting from these defects optical micrographs of the defects were examined where the size of the defects were visually estimated using a nearby Ni strip width as a line scale. The maximum loss of Ni area for a pattern was estimated to be $0.0110 \text{ mm}^2 \pm 0.0002 \text{ mm}^2$ or $2.50 \% \pm 0.04 \%$ of the expected Ni area. The maximum loss of geometric TPB length was estimated to be $960 \text{ }\mu\text{m} \pm 40 \text{ }\mu\text{m}$ or $1.36 \% \pm 0.06 \%$ of the expected TPB. The losses were assumed to have minimal impact on the performance of the anodes and were therefore neglected when normalizing electrochemical measurements with respect to Ni area or geometric TPB length. Overall, the Ni patterns mimicked the geometry of the mask very well, and the desired widths and lengths of the individual strips of the patterns matched the expected dimensions of the mask quite closely (to within $\ll 10\%$). An example of such good agreement is shown in Figure 3.3 which shows an SEM micrograph of a $100 \text{ }\mu\text{m}$ pattern and how its width matches its expected value.

When magnified with SEM imaging, it was revealed that the TPB was composed of jagged edges with roughness of length scales on the order of $2 \text{ }\mu\text{m}$, into the YSZ across the desired TPB. The acid etching procedure gave the pattern edges a jagged shape and therefore the actual TPB length for each pattern was more than the geometric TPB length. The degree to which the TPB matched the specified geometric TPB was be obtained by image processing of the SEM micrographs of Ni pattern edges just after microfabrication, shown in Figure 3.4.

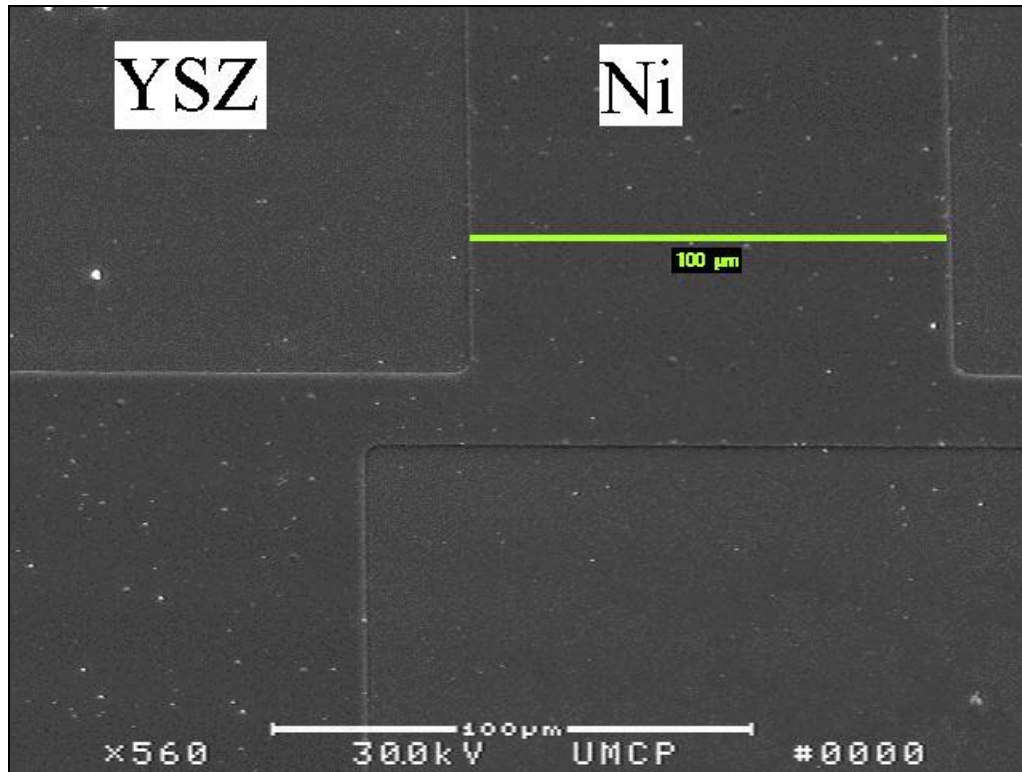


Figure 3.3: SEM micrograph of a 100 μm patterned anode taken just after microfabrication. The 100 μm scaled overlaid shows that specified pattern geometry was achieved.

The crude procedure for estimated actual TPB length describe in section 2.1.2 resulted in large uncertainties due to the relatively large uncertainty of each small line segment's length and the compounding of these uncertainties associated with connecting the line segments end to end. On average 20 line segments were used to approximate the five samples of pattern edges each with geometric TPB lengths of 10 μm . Table 3.1 presents the estimated additional lengths of TPB for the 5 samples of pattern edges calculated using the methodology described in section 2.1.2.

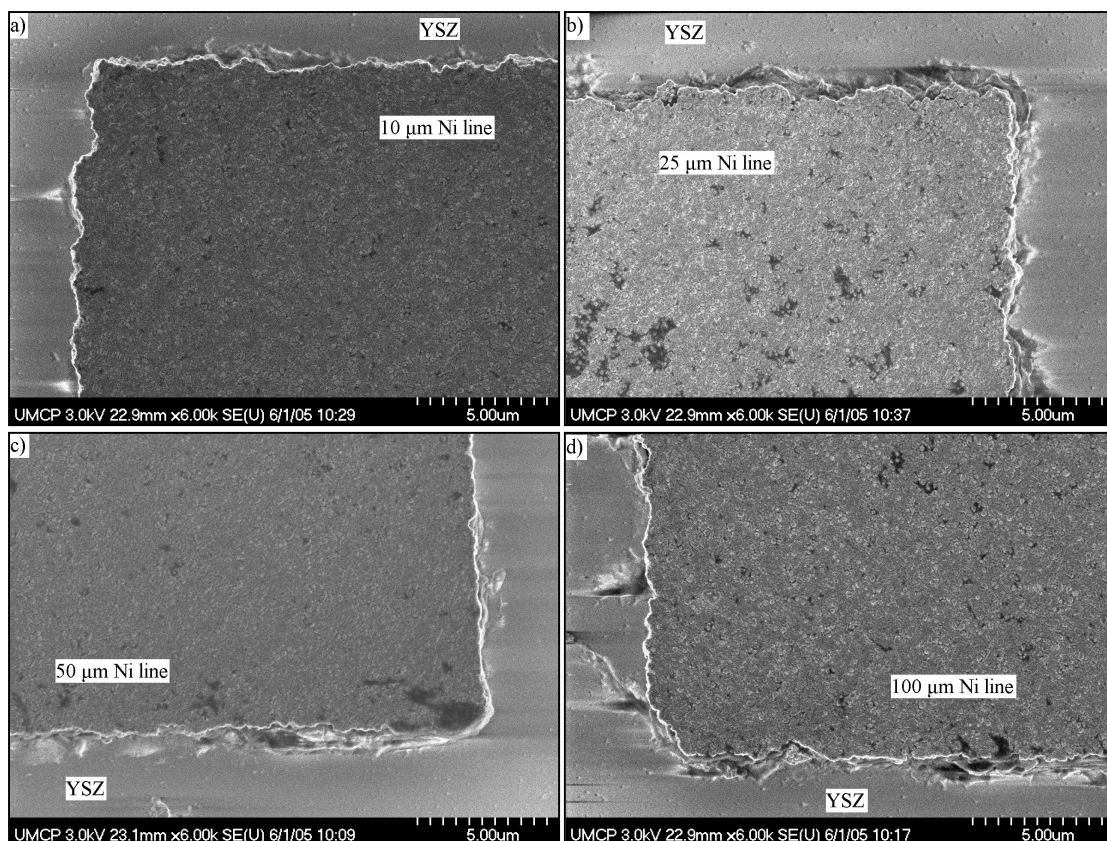


Figure 3.4: SEM micrographs (3450X magnification) of TPB regions from different pattern edges just after microfabrication a) 10 μm b) 25 μm c) 50 μm and d) 100 μm .

Dark colored streaks radiating from the TPB was due to charging effects.

Table 3.1: Additional TPB length from 5 samples of pattern edges as calculated by the methodology described in section 2.1.2.

Sample	Geometric TPB Length [μm]	Addition TPB Length [μm] [*]
1	10.00	0.18
2	10.00	0.12
3	10.00	0.25
4	10.00	0.36
5	10.00	0.10
ave	10.00	0.20

^{*} $\pm 1.60 \mu\text{m}$

The average error involved in the measurements ($\pm 1.60 \mu\text{m} = \pm 0.08 \mu\text{m} \times 20$) was 8 times larger than the average difference between the geometric length and the approximate actual length ($\sim 0.20 \mu\text{m}$). This error ($1.60 \mu\text{m}$) was then taken to be the maximum additional length of the actual TPB length relative to the geometric TPB length. Therefore the actual TPB length was estimated to more than 16 % greater than the geometric TPB length.

The adherence of the patterns to the YSZ was tested using a profilometer before and after electrochemical testing. The profilometer's stylus applied a 10.1 mg force normal to the YSZ surface and translated at $200 \mu\text{m/s}$ from YSZ surface to Ni surface. All patterns, before testing, resisted delamination during the "scratch test", and the ones that remained adhered to the YSZ after testing also resisted delamination. No deformation of the TPB or Ni surface structure caused by the profilometer was observed using the optical microscope.

The patterned anodes from MEA 2 retained their specified geometry and continuity after being heated to 850°C in the reducing H_2/Ar atmosphere (both anode and cathode exposed) for 4 hours. During the heat cycle no electrochemistry took place and therefore there was no flux of oxide ions to the anodes. Optical microscope pictures of a $100 \mu\text{m}$ anode before and after this heat treatment are presented in Figure 3.5.

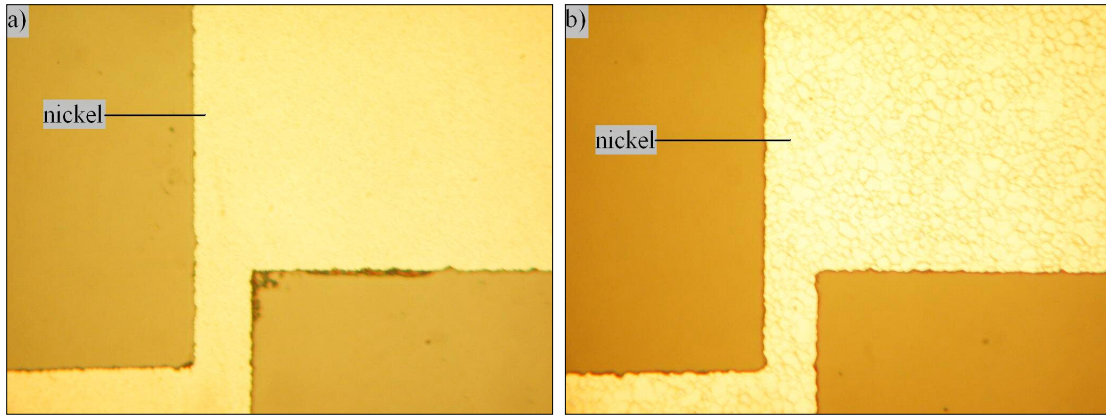


Figure 3.5: Optical microscope pictures (60X magnification) of the 100 μm anode from MEA 2 a) before heat treatment (with dark material being residual photoresist) and b) after heat treatment.

No cracks or pores were observed in the bulk portion of the Ni using a microscope at 60X magnification. However, it was evident that Ni grain growth had occurred; the grain boundaries show up as a web of dark lines in Figure 3.5b. The surface roughness of the Ni increased due to this grain boundary growth. The surface roughness was measured using a profilometer with stylus sweeps 1 mm long. Figure 3.6 shows the paths the profilometer stylus traveled when sampling the pattern profiles. Representative portions of the scans for all anodes taken from MEA 3 (before heat treatment) and MEA 2 (after heat treatment) are shown in Figure 3.7. The y-axis represents the vertical displacement of the profilometer's stylus relative to its initial position on the YSZ surface and the x-axis indicates the displacement of the stylus parallel to the YSZ surface from some arbitrary starting point. The profilometer measured the vertical displacement of the stylus (designated to be y_i), relative to the stylus's initial position (y_l), every 0.4 μm of horizontal displacement.

$y_{YSZ,ave}$ was defined as the average of the first 20 measurements over the YSZ surface and this ‘YSZ baseline’ is set equal to 0 in the profiles in Figure 3.7.

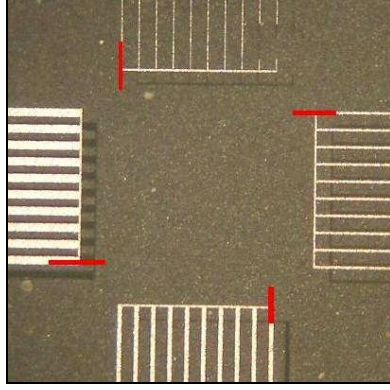


Figure 3.6: Magnified view of anode geometry with red lines showing the path the profilometer’s stylus took when sampling anode profiles.

The profilometry data was used to calculate the Ni coating thickness (h_{Ni} given by equation 3.1), the YSZ surface roughness (δh_{YSZ} given by equation 3.2) and the Ni surface roughness (δh_{Ni} given by equation 3.3).

$$h_{Ni} = \frac{\sum_{i=N-20}^N y_i}{20} - \frac{\sum_{i=1}^{20} y_i}{20} = y_{Ni,ave} - y_{YSZ,ave} \quad (3.1)$$

In equation 3.1 N is the total number of measurements recorded for the scan, $y_{Ni,ave}$ is the average vertical displacement of the stylus relative to its initial position for the last 20 measurements (over the Ni surface) and $y_{YSZ,ave}$ is as previously defined.

$$\delta h_{YSZ} = \sqrt{\sum_{i=1}^{20} (y_i - y_{YSZ,ave})^2} \quad (3.2)$$

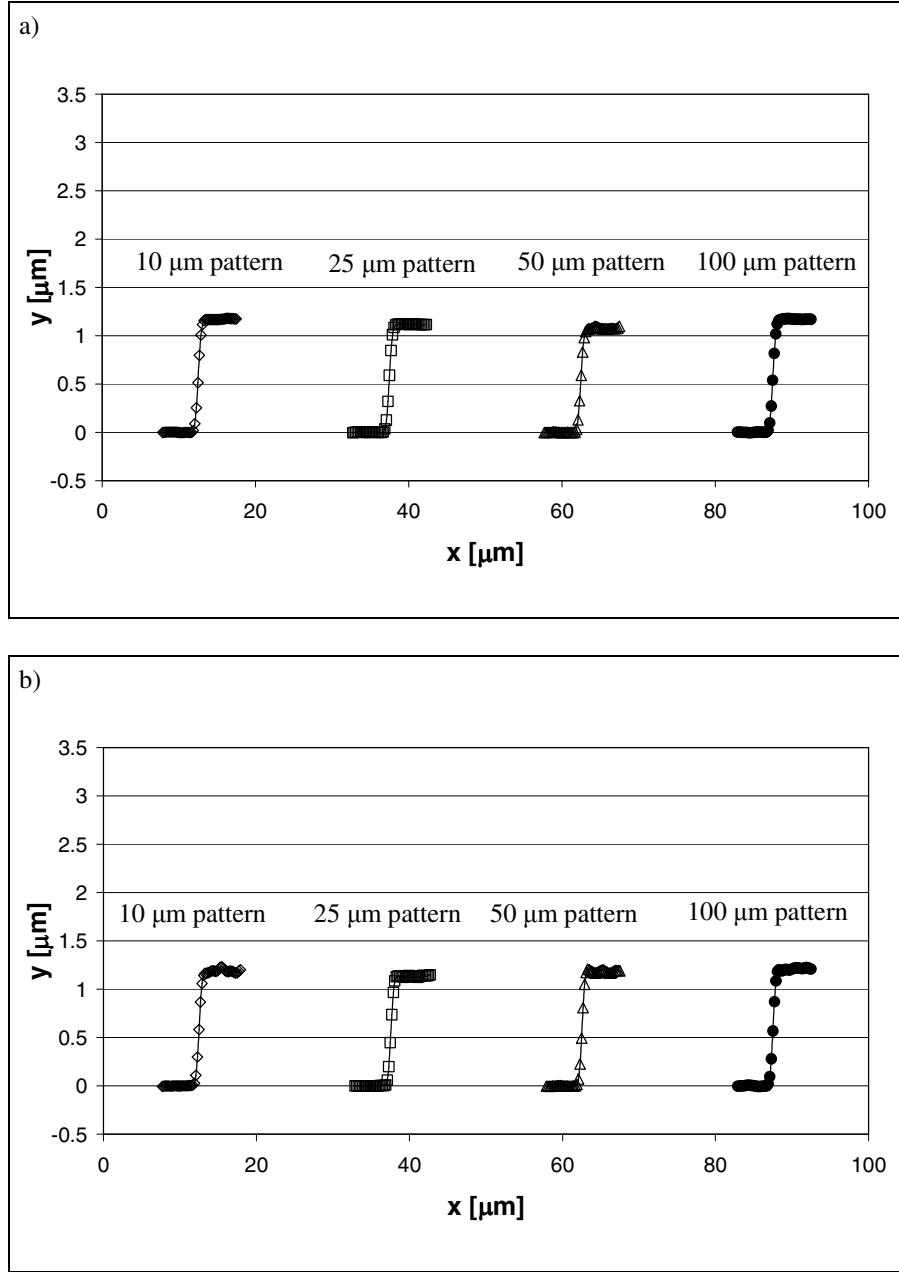


Figure 3.7: Representative anode profiles from a) MEA 3 before heat treatment and b) MEA 2 after heat treatment.

The y_i 's in equation (3.2) are the vertical displacements of the stylus for the first 20 measurements of the scan (over the YSZ surface).

$$\delta h_{Ni} = \sqrt{\sum_{i=N-20}^{20} (y_i - y_{Ni,ave})^2} \quad (3.2)$$

The y_i 's in equation (3.2) are the vertical displacements of the stylus for the last 20 measurements of the scan (over the Ni surface). The Ni coating thickness and roughness values for the MEAs before and after heat treatment are summarized in Table 3.2.

Table 3.2: Profilometry data of the patterned anodes from MEA 3 (before heat treatment) and MEA 2 (after heat treatment).

		10 μm	25 μm	50 μm	100 μm	Ave.
h_{Ni} [nm]	pre-heat	1171	1116	1078	1171	1134
	post-heat	1189	1134	1186	1201	1177
δh_{Ni} [nm]	pre-heat	4.6	4.2	6.8	2.3	4.5
	post-heat	14.3	7.5	10.8	9.2	10.4
δh_{YSZ} [nm]	pre-heat	2.0	1.2	1.4	1.4	1.5
	post-heat	1.6	1.4	1.8	3.3	2.0

The heat cycle increased R_{Ni} by more than two times and the average Ni thickness increased by about 4%. The roughening and slight increase in Ni coating thickness is most likely due to Ni grain growth and grain reconfiguration brought on by the high temperature environment in which the experiment was conducted.

Chapter 4: H₂ Oxidation

As mention in section 2.4 the electrochemical testing of the MEA's operating on H₂ were conducted to provide a baseline to which results from other fuels including CO, CH₄ and other hydrocarbons (in future tests) could be compared. MEA's 1 and 2 were exposed to humidified ($P_{H_2O}/P_{H_2} = 0.05$) H₂ (Table 2.3) for approximately 14 hrs while one anode (either the 100 μm or 50 μm) was polarized ($\eta = 600$ mV or $\eta = 200$ mV) for 8 hrs and the other three were kept at open circuit conditions. In addition, before electrochemical tests were conducted MEA 1 was kept under a high temperature (> 700 °C) reducing H₂/Ar environment (Table 2.3) for over 24 hrs for preliminary testing. Table 4.1 shows the current the polarized pattern (100 μm) from MEA 1 drew at the beginning and end of each period of the experiment (consisting of 40 min of open circuit conditions followed by 2 hr of constant polarization).

Table 4.1: Current drawn by the polarized anode (100 μm) from MEA 1 after open circuit and polarization conditions for each experimental period.

	Current after 40 min of $\eta = 0$ [mA]	Current after 2 hr of $\eta = 600$ mV [mA]
1st Period	7.7*	8.6
2nd Period	7.7	8.2
3rd Period	7.8	8.4
4th Period	7.2	7.6

*Initial current drawn after 24 hrs of open circuit conditions

The current the polarized pattern drew increased by about 0.4 to 0.9 mA while the overpotential was applied, but during each open circuit time period (approximately 40

min) the current decreased to its original value (that after 24 hrs of open circuit conditions) of 7.6 ± 0.4 mA. Assuming that the amount of current drawn from a pattern scales with the length of TPB of the pattern would imply that the 100 μm pattern's length of TPB increased during the times in which it was polarized and decreased during the times in which it was kept under open circuit conditions. TPB lengthening (roughening) and shortening (smoothing) processes have been reported to occur for patterned Ni anodes operating on humidified H_2 and CH_4 fuel feeds.^{16, 36} The TPB lengthening process may be caused by Ni transport to the TPB. In this explanation $\text{Ni}(\text{OH})_2$ is believed to vaporize from the pattern then diffuse to the TPB boundary where the $P_{\text{H}_2\text{O}}/P_{\text{H}_2}$ ratio decreases sharply (during current flow) and $\text{Ni}(\text{OH})_2$ becomes unstable.³⁷ The $\text{Ni}(\text{OH})_2$ breaks down and Ni precipitates out and forms particles at the TPB thereby lengthening the TPB and increasing the amount of current drawn.

The shortening of TPB length, believed to occur during open circuit conditions may be explained by agglomeration of these newly created Ni particles into the bulk Ni grains at the TPB. The high temperatures of the experiment are believed to be responsible for the significant Ni grain growth that occurred (discussed in the next section). The agglomeration of the Ni into these growing grains thereby shortening the length of TPB and decreasing the amount of current drawn.³⁷ The similarities in current values from the first column in Table 4.1 suggests that the same amount of TPB smoothing took place during the 40 min periods of open circuit conditions between periods of polarization as that which occurred when anode was under open

circuit conditions for 24 hrs before the electrochemical test began. Therefore it seems as if the majority of the TPB smoothening process occurs within 40 min for temperatures equal to 800 °C.

The current drawn by the polarized pattern (50 μm) from MEA 2 did not increase during polarization but instead stayed relatively constant (0.6 ± 0.1 mA) throughout the experiment. It may be possible that the overpotential applied to the polarized anode of MEA 2 was not great enough to cause significant Ni transport and associated TPB lengthening. Indeed the study that discusses the $\text{Ni}(\text{OH})_2$ mechanism only saw appreciable increases in current for large anodic overpotentials. For the experimental conditions reported here a $\eta > 200$ mV may be necessary to activate Ni transport to a significant level.

SEM micrographs, shown in Figure 4.1, display the microstructure of the polarized pattern (50 μm) and open circuit patterns (100 μm and 25 μm) from MEA 2. The TPB for the anodes in Figure 4.1 have changed from their original shape (Figure 3.4). Ni grains have grown very large and the TPB is composed of portions of these large Ni grains. Each Ni grain at the TPB contributes about 3 μm of its perimeter to the TPB length and these boundaries are relatively straight and parallel. From visual observation it can be seen that length scales of the TPB's rough features before electrochemical testing, on the order of 2 μm , have been reduced to being on the order of 0.5 μm .

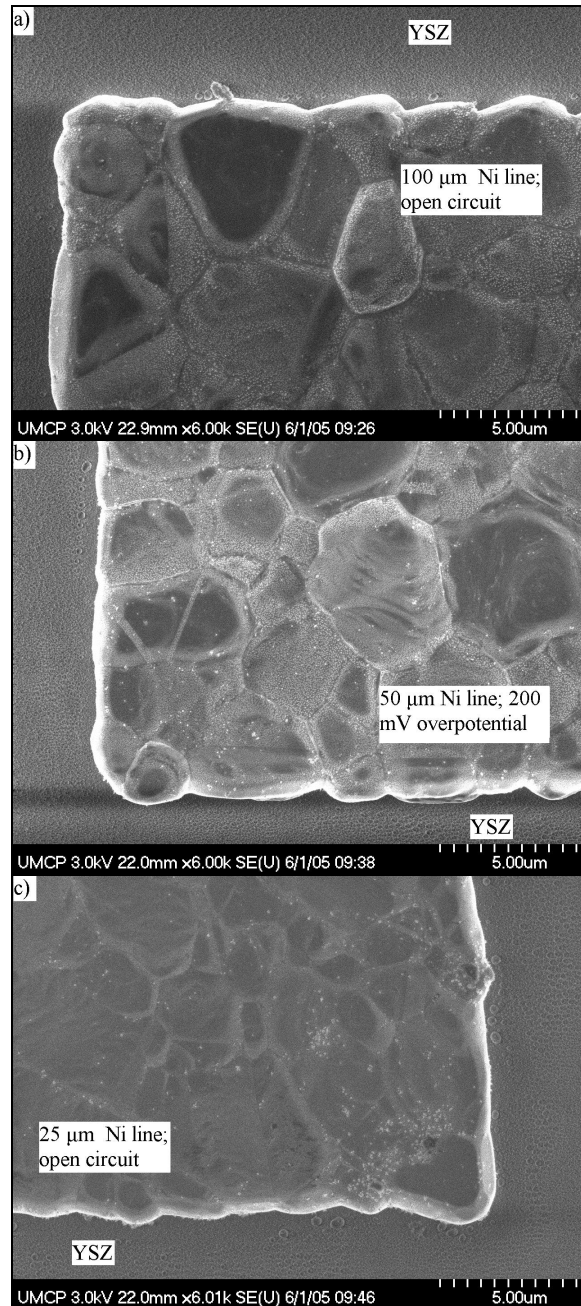


Figure 4.1: Post-experimental SEM micrographs (3600X magnification) from MEA 2 of a) the open circuit 100 μm pattern edge, b) the 50 μm pattern edge after 8 hrs of polarization ($\eta = 200 \text{ mV}$) and c) the open circuit 25 μm pattern edge.

The number of these features has also decreased; this smoothening of the TPB makes the actual TPB lengths approach their geometric values. However, the methodology used to estimate the actual TPB length was not accurate enough to resolve this apparent decrease in length, and so the upper limit on the actual TPB length must be taken as the upper limit of the uncertainty on measured TPB. Similar studies on patterned Ni anodes fabricated via photolithography and wet chemical etching have estimated that actual TPB lengths (after 48 hr in a reducing atmosphere at 700 °C) are no more than 15 % longer than the theoretical ones close to that calculated for this study (16 %).³

Interestingly, the TPB shapes and lengths as well as the size of the Ni grains (4 µm on average) for MEA 2 did not seem to be affected by anode polarization and passage of current. However, the slow cooling of MEA 2 may have masked any effect of overpotential. MEA 2 was kept above 700 °C and under open circuit conditions for over an hour after the final overpotential was removed. The conclusion that appreciable TPB smoothening may occur within 40 min (as discussed above) would indicate that during this cool down time the structure of the polarized anode may have approached that of those kept under open circuit conditions such that any difference was lost.

The profilometry scans of the anodes from MEA 1 and 2 post-electrochemical testing, shown in Figure 4.2, indicate appreciable roughening of the Ni surface. The vertical displacement of the profilometer's stylus relative to its initial position on the YSZ

surface and the x-axis indicates horizontal displacement of the stylus parallel to the YSZ surface from some arbitrary starting point. The open circuit profiles shown are representative of all three open circuit anodes and these anodes have, on average increased in thickness by 20 % relative to the average anode thickness before any testing. Interestingly, the polarized anodes have, on average increased in thickness by 56 % relative to the thickness before testing and have expanded 36 % more than the open circuit anodes. In addition, the polarized anodes are about 8 times rougher than those anodes kept under open circuit conditions. Quantitative data from the scans are presented in Table 4.2.

Table 4.2: Profilometry data of anodes from before any testing (MEA 3) and after electrochemical testing (MEA 1 and 2).

		h_{Ni} [nm]	δh_{Ni} [nm]	% Expansion
MEA 3 pre experiment (ave)		1134	4	-
MEA 1 post experiment	Open circuit (ave)	1581	26	27
	Polarized	1696	249	49
MEA 2 post experiment	Open circuit (ave)	1280	52	13
	Polarized	1850	404	63

The dramatic increase in surface roughness of the polarized anodes relative to the open circuit anodes may be explained by Ni oxidation. During the periods in which an overpotential was applied to the polarized patterns there was a steady flux of O^{2-} ions to the Ni/YSZ interface. The O^{2-} ions that arrived at the TPB would most likely be consumed in charge transfer reactions with H_2 and so may not have oxidized the Ni in this region.

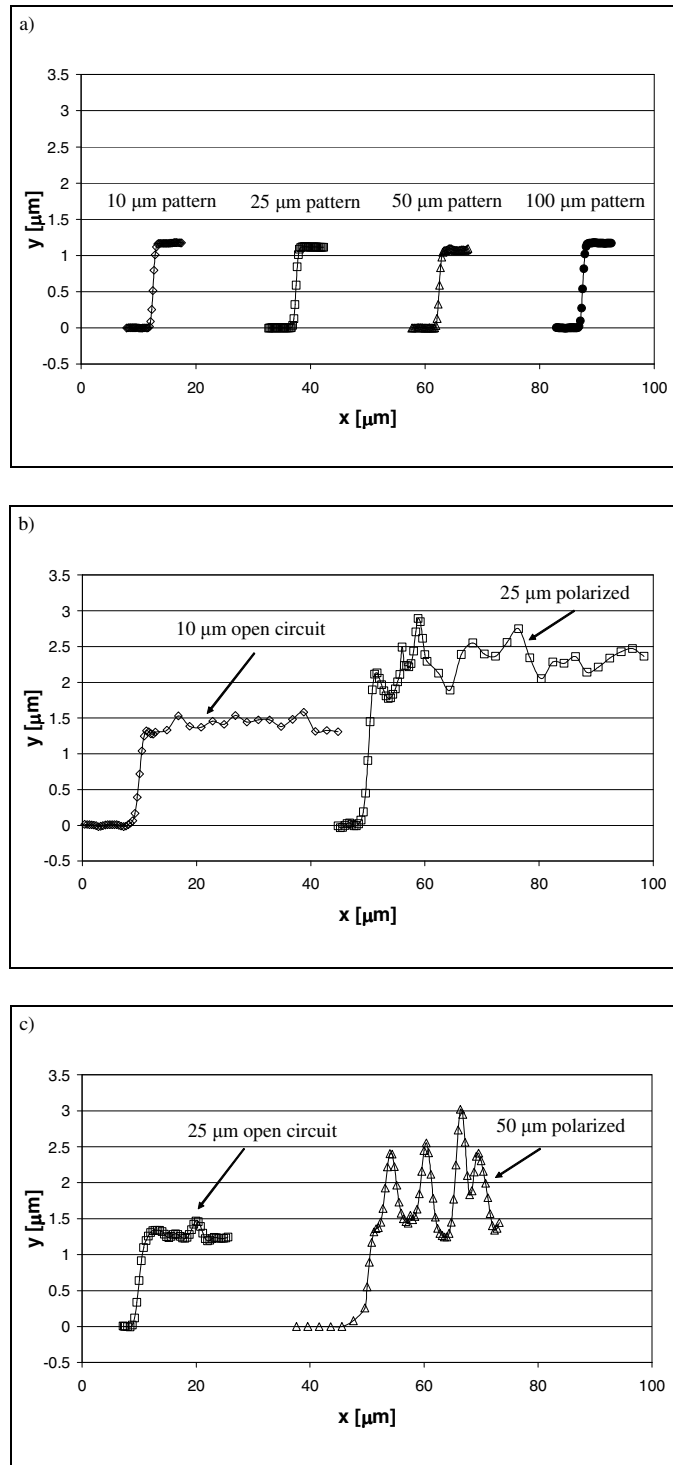


Figure 4.2: Profilometry results from a) MEA 3 just after anode fabrication, b) MEA 1 after electrochemical testing and c) MEA 2 after electrochemical testing. Scan paths are shown in Figure 3.6.

This may explain the relatively smooth TPB seen in the SEM micrographs of Figure 4.1. However O^{2-} ions at the Ni/YSZ interface in the interior of the pattern may have become incorporated into the bulk Ni. The growth and reconfiguration of pure Ni grains along with the formation of NiO, possibly as islands spread throughout the interface, may explain the expansion of the Ni coating and roughening of the Ni surface. Fully dense NiO samples are theoretically predicted to expand 69.2 % during oxidation³⁸ close to that seen in this study (56 %).

The results from EIS for the open circuit pattern (10 μm) and polarized pattern (50 μm) from MEA 2 at the beginning and end of the electrochemical experiment are shown in Figure 4.3.

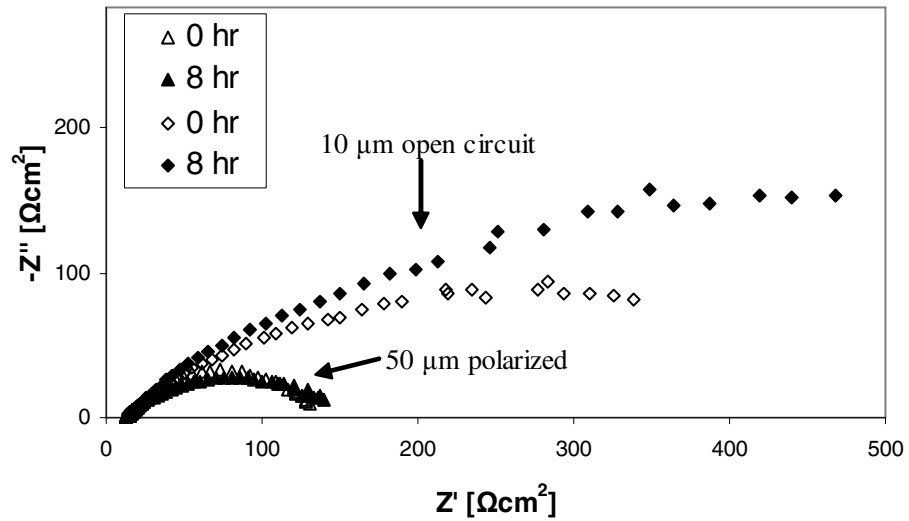


Figure 4.3: Impedance curves for the open circuit (10 μm) and polarized (50 μm) patterns from MEA 2 before and after electrochemical testing ($\eta = 200$ mV for 8 hr).

Although the low frequency real-axis intercept for the open circuit anode was not recorded (in order to speed up the data recording process) it can be seen that after approximately 12 hours of open circuit conditions the total cell resistance of the open circuit anode increases. Conversely, the total cell resistance of the polarized anode increases only slightly (7 %) over the course of the experiment. The change or lack of change in total cell resistance for both anodes can also be seen by examining the V - i curves for both patterns as shown in Figure 4.4.

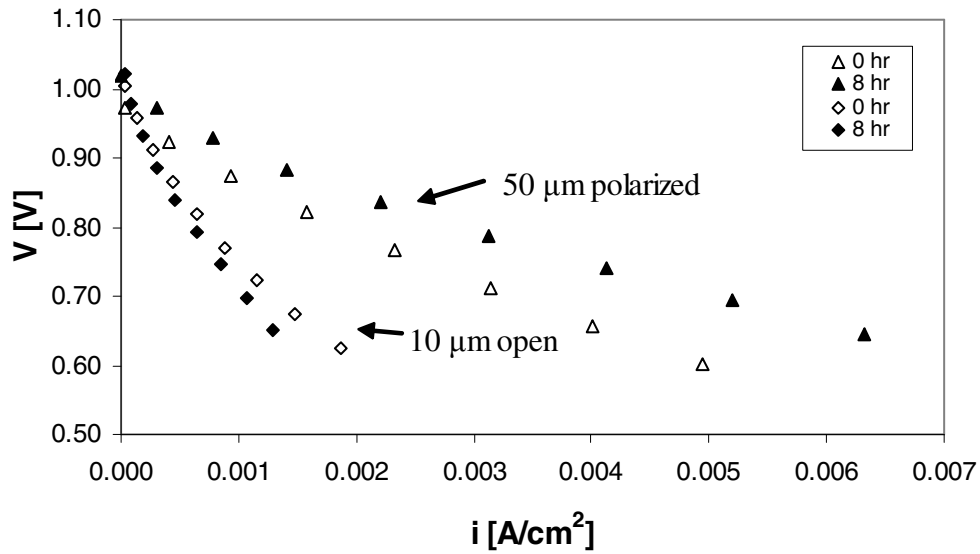


Figure 4.4: V - i curves (with I^*R_b subtracted) of the open circuit (10 μm) and polarized (50 μm) patterns from MEA 2 before and after electrochemical testing ($\eta = 200$ mV for 8 hr).

The initial slope of the polarized anode (i.e., an approximate anodic charge transfer resistance, R_{CT}) does not change much after 8 hrs of polarization although there is improvement in performance at overpotentials greater than approximately 100 mV.

However, the initial slope or approximate R_{CT} of the anode kept under open circuit conditions for 12 hrs increases as a function of time and its performance is worse at the end of the experiment at all overpotentials.

The formation of a NiO layer between the Ni and YSZ surface mentioned earlier may explain the relatively constant total cell resistance seen for the polarized anode. It has been reported that the (111) NiO // (100) ZrO₂ interface exhibits good coherency across the interface boundary that consists of a shared oxygen plane.³⁹ This NiO/YSZ interface may improve the adherence of the pure Ni to the YSZ. In addition the bulk resistance of the polarized anode increases 17 % (vs. 3 % for the open circuit anode) after the 8 hrs of polarization, which may be resultant of an increase in resistance to electron flow with the increased NiO content in the pattern. Furthermore, an increase in total cell resistance of the 10 μ m pattern may be explained by an increase in interfacial resistance between the Ni and YSZ. Without a layer of NiO forming between the open circuit anode and YSZ the anode may not adhere as well to the YSZ and partially delaminate. After removal of MEA 2 from the experimental rig the 10 μ m and 25 μ m patterns were seen to have delaminated from the YSZ possibly this delamination was initiated during the experiment and exacerbated during the cool down of the MEA to room temperature.

The optical and SEM micrographs of the patterned Ni anodes just after microfabrication show that the Ni deposition and photolithographic procedure developed in this study produce high quality patterned Ni anodes with TPB lengths

and Ni/YSZ contact area that can be characterized. The quality of the polarized pattern, including TPB length, Ni surface roughness and adherence to the YSZ, after electrochemical testing with H₂, was also characterized. The SEM micrographs of the anode edges after the test show that the TPB lengths had been reduced due to Ni grain growth but still could be approximated to be no more than 16% longer than the geometric TPB lengths. The profilometry measurements before and after electrochemical testing reveal that the surface of the polarized anode becomes much rougher than those anodes kept at open circuit conditions and that the adherence of this anode to the YSZ was strong enough to withstand the profilometer “scratch test”. The relatively constant total cell impedance of the polarized anode also suggests that this anode maintained adherence to the YSZ implying that polarization has a positive impact on anode stability.

Chapter 5: CO Oxidation

SOFC's with Ni-based anodes have shown sustained operation on humidified CO fuel feeds as mentioned in section 1.2. The addition of steam in an external reformer or the anode chamber of an SOFC will convert a hydrocarbon fuel flow into a mixture of fuels including CO. Therefore understanding the electrochemical oxidation of CO is important for understanding the performance of SOFC's operating on hydrocarbon fuel flows.

MEA 5 was exposed to humidified ($P_{H_2O}/P_{CO} = 0.05$) CO ($P_{CO} = 0.33$) (Table 2.3) for approximately 11 hours while the 100 μm pattern was polarized ($\eta = 200 \text{ mV}$) for 6 hrs and the other three anodes were kept under open circuit conditions. The polarized and open circuit anodes followed the same trends as those from the H_2 tests. As seen in Figure 5.1 the total cell resistance for the polarized pattern (100 μm) stayed relatively constant throughout the course of the experiment with only an increase in R_b of 16 % and a slight decrease in R_p . However, the total cell resistance for the open circuit pattern (10 μm) increases relative to its initial total cell resistance.

Contrary to what is reported in the literature the total cell resistances for both the polarized and open circuit anodes from MEA 5 operated on CO are smaller than those from MEA 2 operated on H_2 (Figure 4.3).¹¹ The geometry of the polarized patterns and the electrolyte thickness varies between the two experiments but the exact reason for the apparent improvement in performance for the anodes operated on CO is not

yet fully understood and further investigations are being conducted with patterned Ni anodes operating on H₂ and CO fuel feeds.

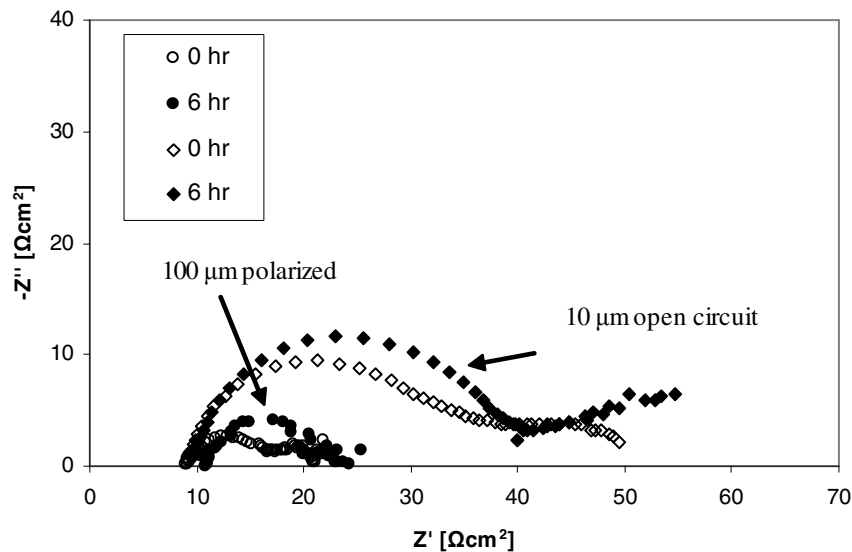


Figure 5.1: Impedance curves of the polarized (100 μm) and open circuit (10 μm) patterns from MEA 5 before and after electrochemical testing.

The behavior of these anodes is reflected in their $V-i$ curves, shown in Figure 5.2. The initial slopes of the $V-i$ curves for the polarized anode stay relatively constant as does its performance at higher overpotentials whereas the performance of the open circuit anode is observed to decrease as a function of time. The relatively constant total cell resistance of the polarized anode from MEA 5 may be due to the formation of NiO between the Ni and YSZ (as proposed for the H₂ test) improving adherence between the Ni and YSZ. Post-experimental EDAX analysis, shown in Figure 5.3, was performed on the Ni strip of the polarized pattern from MEA 5.

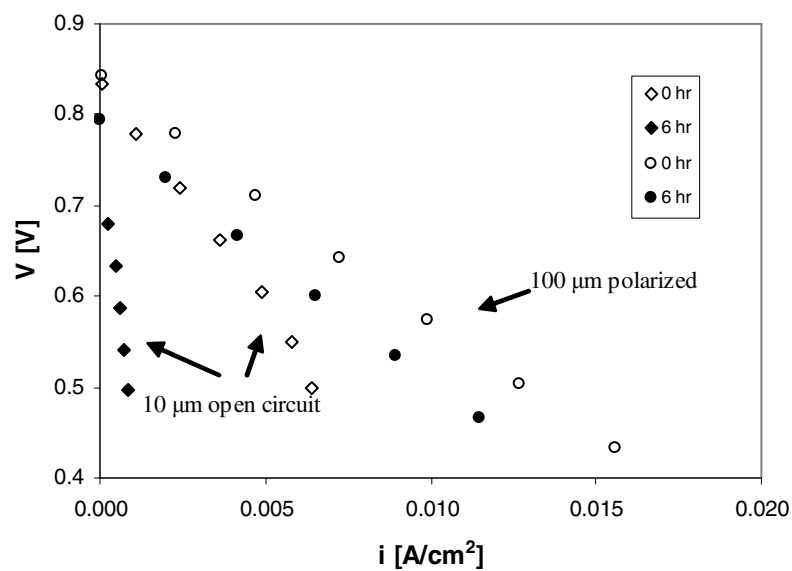


Figure 5.2: V - i curves (with $I \cdot R_b$ subtracted) for the polarized (100 μm) and open circuit (10 μm) patterns from MEA 5 before and after electrochemical testing.

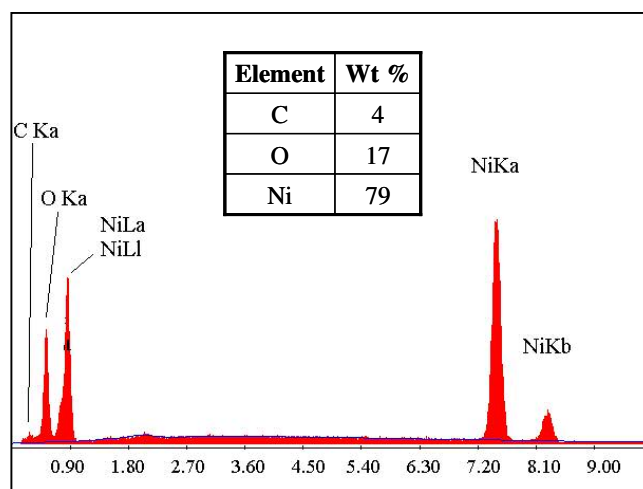


Figure 5.3: EDAX pattern from the center of a Ni strip from the polarized pattern (100 μm) from MEA 5 after electrochemical testing.

Only a slight amount of carbon (4 wt %) of carbon detected on the surface of the Ni as was expected for this polarized pattern. Raman spectra also showed the presence of carbon as well as OH and H species bonded to the Ni surface as shown in Figure 5.4.

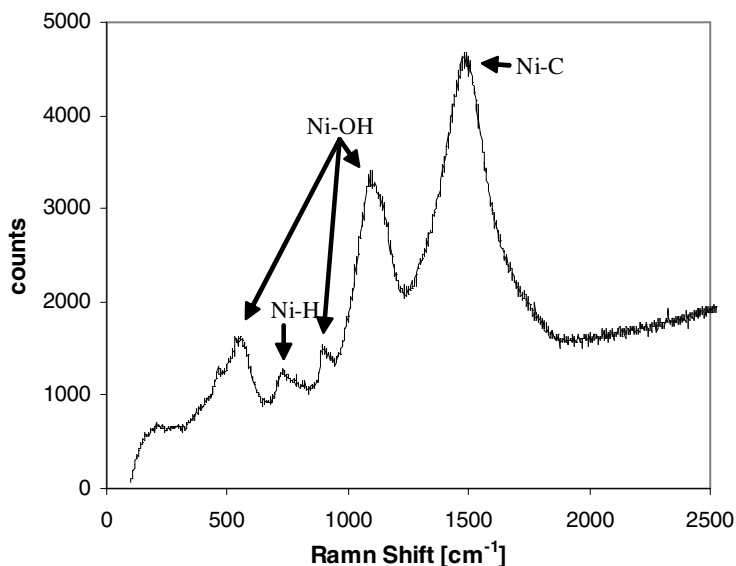


Figure 5.4: Raman data of the polarized pattern (100 μm) from MEA 5 post-electrochemical testing.

The large peak near 1484 wavenumbers signifies the presence of non-graphitic carbon clusters, those near 1097, 897, and 548 wavenumbers are Ni-OH bond stretches, and that peak near 728 wavenumbers is a Ni-H bond stretch.³⁴ This MEA was cooled under Ar only after the electrochemical testing in hopes that the OH and H surface intermediate species would maintain a presence on the Ni surface during the MEA cool down under the Ar flow. The presence of significant OH on the Ni surface suggests that water adsorption may play a role in the electrochemistry.

Furthermore, the possibility of equivalent surface water gas-shift ($\text{CO(s)} + \text{OH(s)} \rightleftharpoons \text{CO}_2\text{(s)} + \text{H(s)}$) on the Ni catalysts seems likely which can explain the relatively low amount of carbon deposition on the Ni for the test conditions.

The EDAX results from Figure 5.4 also show that 17 wt % atomic oxygen was present in the Ni pattern implying the formation of NiO. The lack of a peak for yttrium or zirconium indicates that the Ni pattern was thick and dense enough to block X-rays from reaching the YSZ and so oxygen was not detected from any yttria of zirconia. XRD analysis in the center of a Ni strip of the polarized pattern after the electrochemical testing revealed the presence of NiO as shown by the X-ray pattern in Figure 5.5.

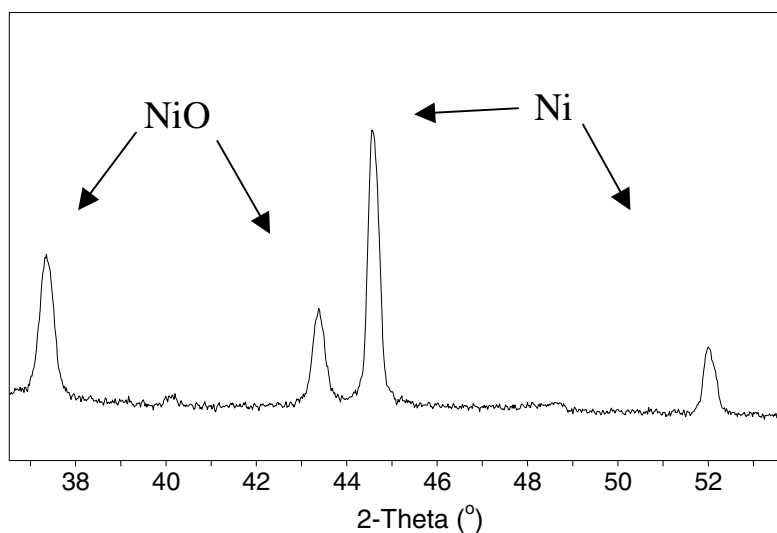


Figure 5.5: X-ray pattern from the center of a Ni strip from the polarized pattern (100 μm) from MEA 5 after electrochemical testing.

The peaks near 37° and 43° signify the presence of NiO and those peaks near 44.5° and 52° are those associated with Ni. The formation of NiO at the Ni/YSZ interface may also help to explain the surface roughening for the polarized pattern (100 μm) as seen in the post-experimental SEM micrographs of Figure 5.6.

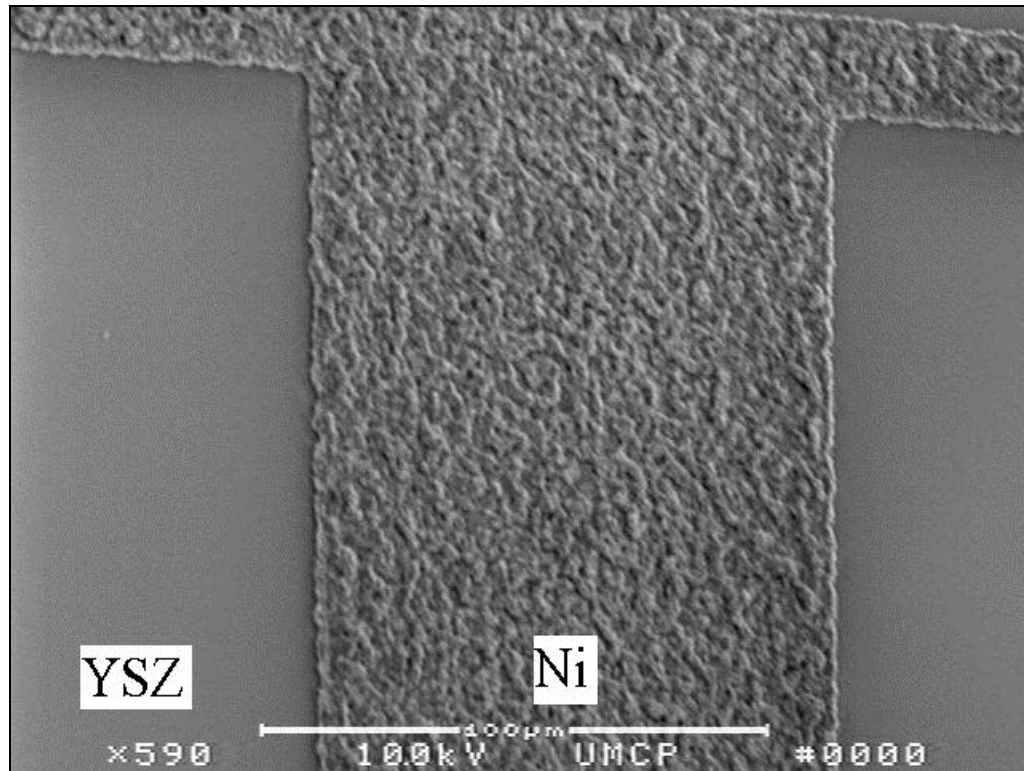


Figure 5.6: Low magnification (1670X magnification) SEM micrograph of the polarized anode (100 μm) from MEA 5 after electrochemical testing.

It is likely that here as well as for the H_2 test that Ni grain growth and reconfiguration contributes to the change in surface structure. However, the Raman, EDAX and XRD data suggest that NiO has become present in the polarized Ni pattern. As explained previously, the relatively constant total cell resistance and roughening of the Ni surface may be due to a NiO layer forming between the Ni and YSZ which improves

the adherence between the Ni and YSZ and pushes up and reconfigures Ni grains increasing the Ni surface roughness. On the other hand, the Ni oxidation is not complete and a layer of Ni metal on the surfaces and edges of the patterns still provides adequate electronic conductivity and surface activity to maintain the relative constant resistances for the patterns after electrochemical exposure.

The polarization of the patterned Ni anode operated on humidified CO has a positive effect on total cell resistance as was also seen in the H₂ test. It is proposed that the formation of NiO between the Ni and YSZ improves anode adherence to the YSZ as well as increases the roughness of the Ni surface. The polarized pattern has demonstrated the ability to resist uncontrolled carbon deposition over the course of the experiment (~ 10 hr). The addition of water and the applied overpotential likely kept the Ni surface free of appreciable carbon depositions possibly through an equivalent water gas-shift reaction occurring on the Ni surface.

Chapter 6: CH₄ Oxidation

CH₄ is a more practical fuel than either H₂ or CO and is also formed when heavier hydrocarbon fuels undergo reforming. Therefore patterned anode performance on humidified CH₄ fuel feeds can give important information that is necessary to the development of SOFC anodes that can sustain operation on heavy hydrocarbon fuel feeds.

MEA's 3 and 4 were both exposed to humidified ($P_{H_2O}/P_{CH_4} = 0.05$) CH₄ ($P_{CH_4} = 0.33$) (Table 2.3) for approximately 11 hours while either the 50 μm (MEA 2) or 25 μm (MEA 3) pattern was polarized ($\eta = 100$ or $\eta = 80$ mV, respectively) for 6 hrs and the other three anodes were kept under open circuit conditions. The electrochemical impedance curves, shown in Figure 6.1, of the polarized (25 μm) and open circuit (10 μm) anodes from MEA 4 show trends similar to those seen in the H₂ and CO tests.

The total cell resistance of the open circuit pattern is observed to increase as a function of time similar to the results observed in the other two experiments.

However, in this experiment the total cell resistance of the polarized anode approximately doubles in the last 6 hrs of the experiment. The voltammetry results plotted in Figure 6.2 show a slight increase in initial slope of the polarized pattern and a greater decrease in initial slope of the open circuit pattern.

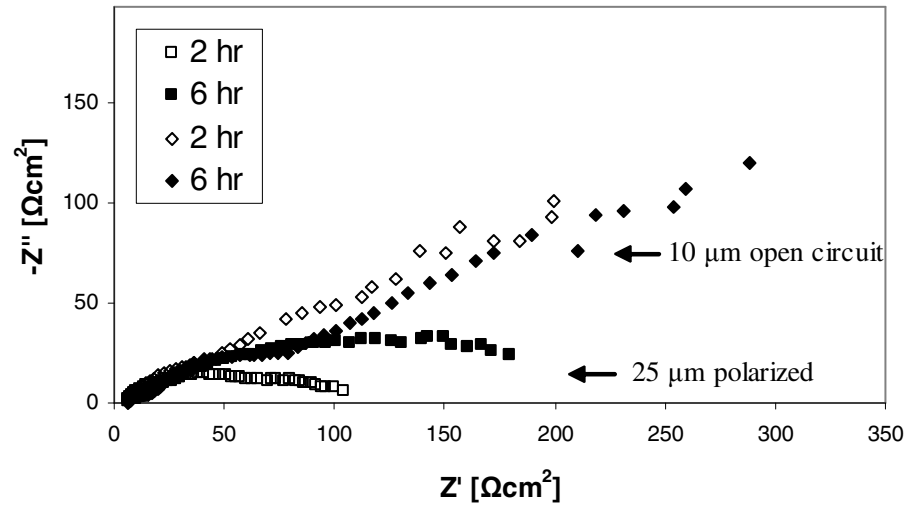


Figure 6.1: Impedance curves of the polarized (25 μm) and open circuit (10 μm) patterns from MEA 4.

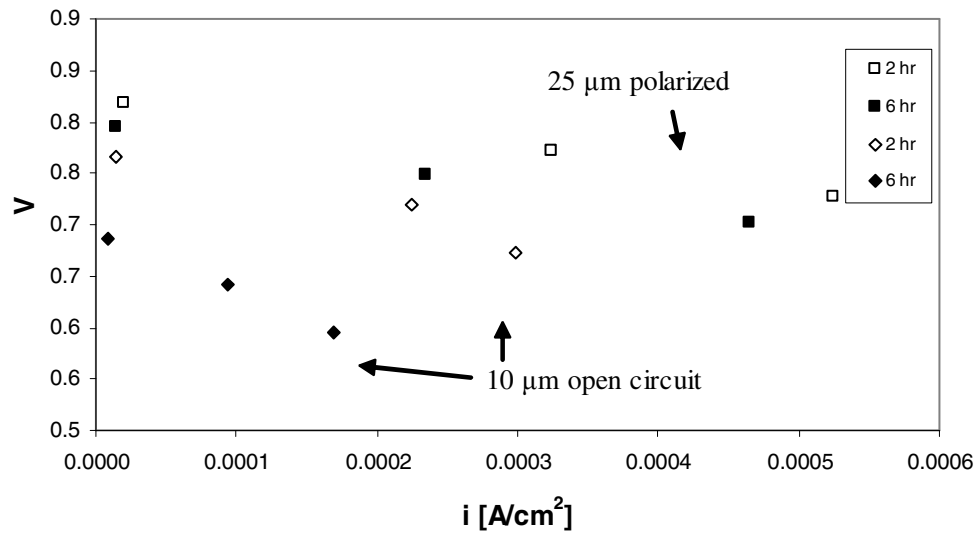


Figure 6.2: $V-i$ curves (with $I \cdot R_b$ subtracted) of the polarized (25 μm) and open circuit (10 μm) patterns from MEA 4.

The degradation in performance of the polarized anode is also apparent in Table 6.1 which presents the current the polarized pattern drew after residing at open circuits for 40 mins and after 2 hrs of polarization for each experimental period.

Table 6.1: Current drawn by the polarized anode (50 μm) from MEA 3 after open circuit conditions and polarized conditions

	Current after 40 min of $\eta = 0$ [mA]	Current after 2 hr of $\eta = 600$ mV [mA]
1st Period	0.23	0.21
2nd Period	0.16	0.10
3rd Period	0.05	0.02

The increase in total cell resistance of the open circuit anode may again be explained by partial delamination of the anode but the increase in total cell resistance of the polarized anode is not believed to be due to delamination. As discussed for H_2 oxidation in Chapter 4 $\text{Ni}(\text{OH})_2$ is reported to form for CH_4 fuel feeds for large oxygen potentials.¹⁶ However, no increase in current drawn by the polarized pattern was observed. Instead the current continually decreases during polarization and open circuit time periods. The lack of improvement in performance during polarization periods may be because an $\eta > 200$ mV is necessary to accomplish appreciable Ni transport and TPB lengthening as proposed in Chapter 4 for the H_2 test on MEA 2 where the applied overpotential of $\eta = 200$ mV did not cause improvement in anode performance during periods of polarization.

An alternative explanation can be an excessive build-up of surface carbon due to the low steam to carbon ration. As reported in the literature a steam to carbon ratio > 2 is

necessary to avoid uncontrollable carbon deposition.¹¹ The excessive surface carbon can lower diffusion of active species to the TPB and block adsorption sites for activated CH₄ adsorption on the Ni as suggested by steam reforming studies of CH₄ on Ni.^{17, 40} The continued degradation of the current during open circuit conditions indicates that carbon deposition is more significant for the CH₄ than for the CO oxidation, and thus is likely leading to the blocking of electrochemical sites and degrading performance during periods of polarization as well as open circuit conditions. EDAX analysis of the current collector bar from the polarized pattern (50 µm) from MEA 3, shown in Figure 6.3, indicated the presence of 12 wt % carbon which is significantly higher than for the CO oxidation anodes.

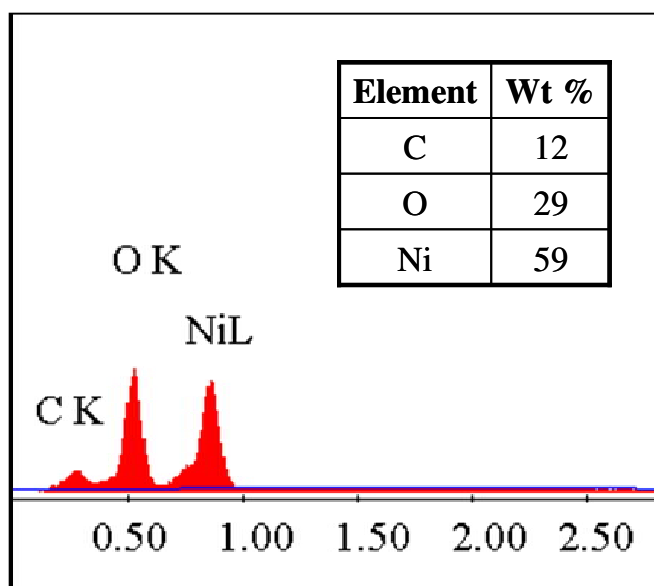


Figure 6.3: EDAX results from the current collector bar of the polarized pattern (50 µm) from MEA 3.

On the other hand, EDAX analysis performed on the YSZ approximately 50 μm away from the polarized pattern found 53 wt % carbon implying that oxidation or reforming reactions may have been taking place on the Ni surface (as proposed for the CO fuel flow) thereby reducing the amount of carbon that deposited on the Ni anode. Raman measurements of the current collector bar from the polarized pattern from MEA 3 also indicated the presence of carbon as well as OH and H species bonded to the Ni surface as shown in Figure 6.4.

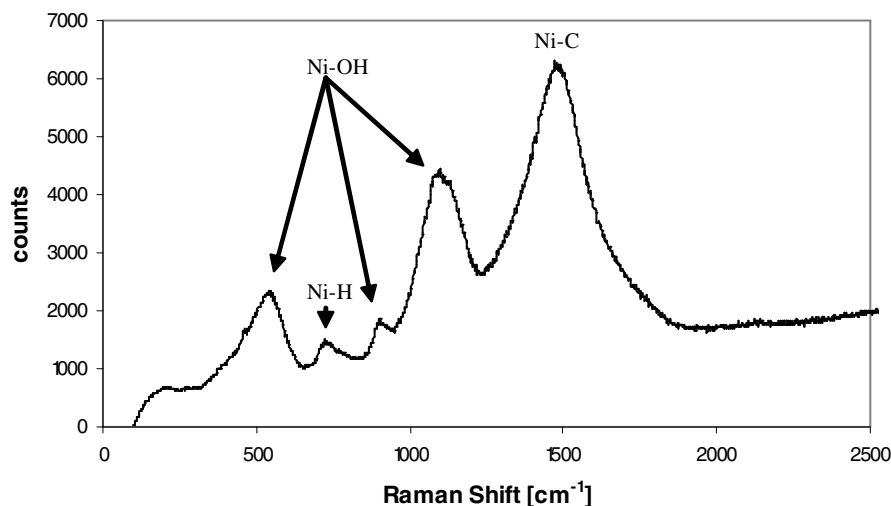


Figure 6.4: Raman of the current collector bar from the polarized pattern (50 μm) from MEA 3.

The peak locations are almost identical to that recorded for the CO test. The large peak near 1486 wavenumbers signifies the presence of non-graphitic carbon clusters, those near 1099, 898, and 552 wavenumbers are Ni-OH bond stretches, and that peak near 732 wavenumbers is a Ni-H bond stretch.³⁴ As proposed for the CO experiment

these OH and H species may have been charge transfer reaction intermediates that “froze” to the Ni surface during cool down possibly explaining the lower amount of carbon that deposited on the Ni relative to the non-active YSZ.

The EDAX results from Figure 6.3 also indicated that 29 wt % oxygen was present in the Ni current collector bar implying that NiO may also have formed under these experimental conditions. Profilometry data collected from MEA 4 after electrochemical testing, shown in Figure 6.5, follows the trend seen in the H₂ experiment. The polarized pattern expanded 100 % relative to the pre-experimental thickness and 78 % more than the open circuit anode and the roughness of the polarized pattern is about 2.5 times that of the open circuit pattern. The expansion is larger than what can be explained by Ni oxidation and this suggests that carbon deposition may be significant for the CH₄/Ni/YSZ system at these low steam to carbon ratios. The quantitative data obtained from the profiles is summarized in Table 6.2. Again, a larger increase in roughness of the polarized anode is seen as in the H₂ experiments. This may be explained by oxidation of the Ni at the Ni/YSZ interface due to the constant flux of O²⁻ imposed on the polarized patterns throughout the course of the experiment. The Ni grain growth and grain reconfiguration associated with the high temperatures of the experiment and the possible formation of NiO islands between the Ni and YSZ may explain the greater Ni coating expansion and increase in surface roughness for that anode kept under a constant overpotential relative to those kept under open circuit conditions. On the other hand, in these

experiments more significant growth of the non-polarized pattern suggests that carbon deposition is likely at work as well.

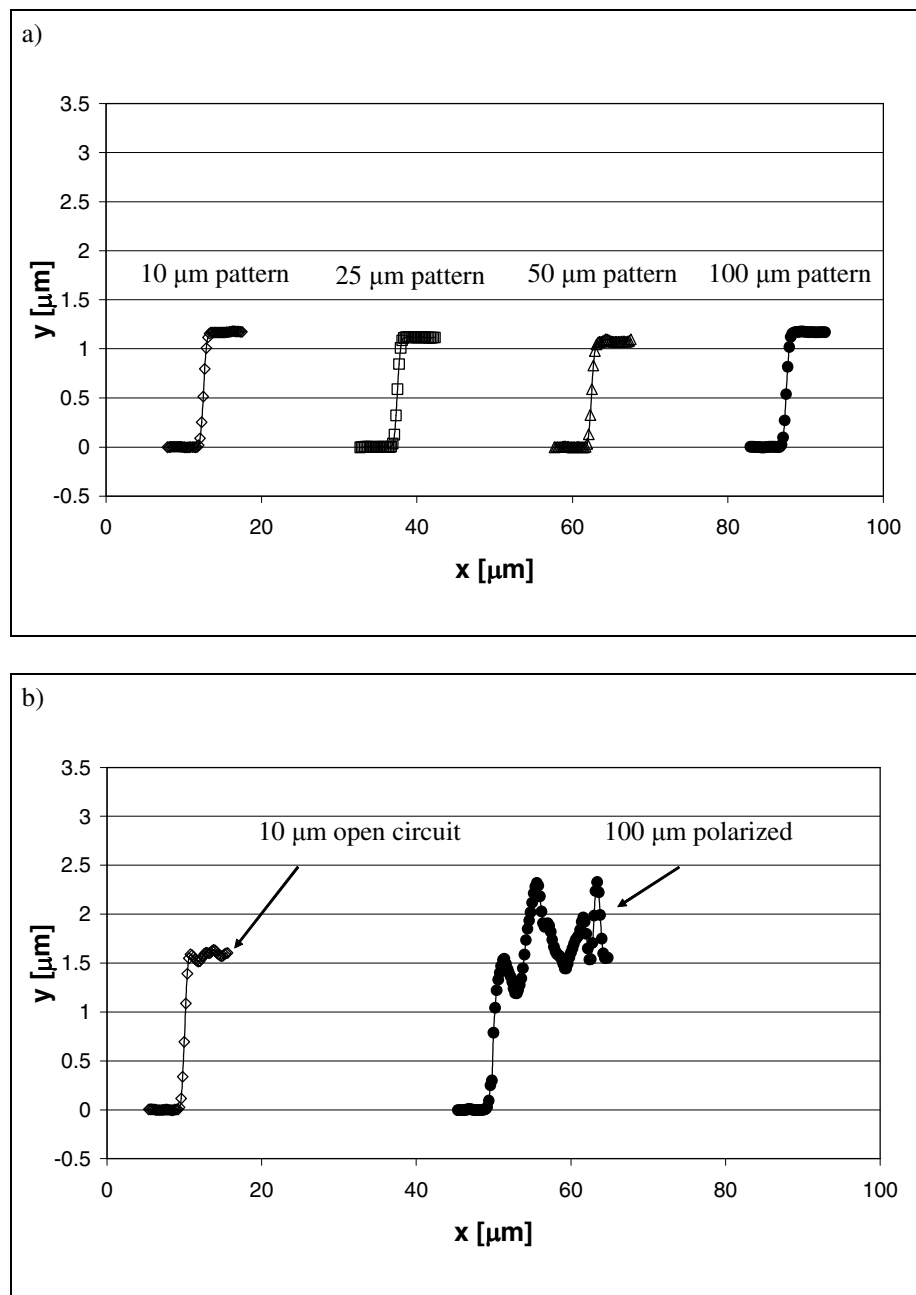


Figure 6.5: Anode profiles a) before electrochemical experiment (MEA 3) and b) after electrochemical experiment (MEA 4). Scan paths are shown in Figure 3.6.

Table 6.2: Profilometry data of the anodes from before (MEA 3) and after (MEA 4) experimental testing.

		h_{Ni} [nm]	δh_{Ni} [nm]	% Expansion
MEA 3 pre experiment (ave)		1134	4	-
MEA 4 post experiment	Open circuit (ave)	1380	87	22
	Polarized	2266	221	100

The characterization of the patterned Ni anode surface roughness was possible after the electrochemical test with humidified CH₄. The polarized pattern was found to increase in roughness about two times more than the open circuit anode implying that overpotentials have a significant effect on the structure of the patterned Ni anode. Ni grain growth and reconfigurations explains some roughening but surface species measurements pointed to the presence of carbon and NiO which may also have had a role in the increase surface roughness. The total cell resistance for the polarized pattern operated on humidified CH₄ was found to increase in time in contrast to the H₂ and CO tests implying that the carbon (detected by the surface species measurements) may have been degrading anode performance and that a higher content of steam or larger overpotential may be necessary to reduce carbon deposition and improve anode stability.

Chapter 7: Conclusions

Patterned Ni anodes exposed to a high temperature (800 °C) reducing environment ($\text{H}_2\text{-Ar}$) for a short period of time (4 hr) without any electrochemistry taking place causes TPB length shortening due to agglomeration of the roughness features of the jagged TPB shape and Ni grain growth. The Ni grain growth and reconfiguration also seems to increase the roughness of the Ni surface and which is most likely resultant from the high temperature environment in which the experiment was conducted.

The lesser amount of carbon on the Ni surface of those polarized anodes operating on CO and CH_4 as well as the presence of H and OH species may indicate that charge transfer reactions occur on the Ni surface that slow the process of carbon deposition. In addition they support the idea that Ni may be transmitted to the TPB as $\text{Ni}(\text{OH})_2$ for polarized Ni anodes operating on $\text{H}_2/\text{H}_2\text{O}$ atmospheres thereby increasing TPB length and anode performance. This phenomenon is proposed to compete with the TPB smoothening process mentioned above.

Roughening of the Ni surface as well as expansion of the Ni coating was seen for patterns exposed to H_2 , CO and CH_4 at 750 °C for prolonged periods of time (≥ 12 hrs) in which electrochemistry was occurring. Interestingly, the patterns that received a constant overpotential for the majority of the electrochemical experiment showed a significant increase in surface roughness when compared to those patterns kept under open circuit conditions. It is believed that the oxide ion flux to the polarized pattern

caused oxygen to incorporate itself into the nickel to form NiO at the Ni/YSZ interface. This proposal is supported by the post-experimental Raman, EDAX, and XRD analysis of tested anodes. The formation of NiO may explain the increase in coating thickness and surface roughness observed as well as the relatively constant total cell resistance seen for the polarized patterns operating on H₂ and CO. The NiO layer may have helped these Ni patterns adhere to the YSZ throughout testing. Contrastingly, the total cell resistance of the open circuit anodes was observed to increase as a function of time. These anodes may have been delaminating due to a lack of NiO formation thereby increasing their interfacial and total cell resistance.

Patterned Ni anodes operating at typical SOFC overpotentials and on humidified H₂ and CO fuel feeds have shown to have relatively constant total cell resistances. The polarized patterned Ni anode operating on humidified CH₄ have shown a slow increase in total cell resistance as a function of time most likely due to carbon formation. However, all the polarized patterns maintained their adherence to the YSZ and had quantifiable TPB lengths before and after electrochemical testing. This indicates that in future studies electrochemical data collected using patterned Ni anodes can be used to elucidate the kinetics and mechanisms of Ni anodes utilizing H₂, CO and CH₄ fuel feeds.

It is recommended that further studies on patterned Ni anode stability in SOFC conditions be conducted. For the future studies the humidified fuels (H₂, CO and CH₄) and the overpotentials applied to the anodes should be the only experimental

variables. In other words MEA's should have equal electrolyte thicknesses and should be tested at the same temperatures and for an equal amount of time so as to elucidate only the effect of overpotential and fuel species. It is also recommended that four electronically independent pattern anodes with equal geometry be tested, i.e. equal Ni/YSZ contact area and equal TPB length. Different overpotentials ($\eta = 0, 200, 300$ and 400 mV) should be applied to each pattern in consecutive time periods, as was done in this study, separated by quick and simultaneous EIS and sweep voltammetry measurements for all anodes. Using this procedure one could isolate the effect of varying amounts of overpotential for each fuel studied. It is also recommended that in situ Raman spectroscopy measurements be conducted to obtain information on what species exist on the Ni and YSZ surfaces during the electrochemical testes. This information would further the understanding of what electrochemical mechanisms are taking place at the anodes and how these mechanisms effect anode stability. Conducting these revised experiments with the addition of in situ Raman measurements will further the understanding of pattern Ni anode stability in SOFC conditions. This will allow for accurate interpretation of experimental data collected using the patterned Ni anodes and subsequent understanding of electrochemical oxidation kinetics for various fuels in Ni-based anodes.

Appendix A. Patterned Ni Anode Defects

Only three localized pattern defects were detected after anode microfabrication for the 5 tested MEAs. The defects are presented in Figure A.1.

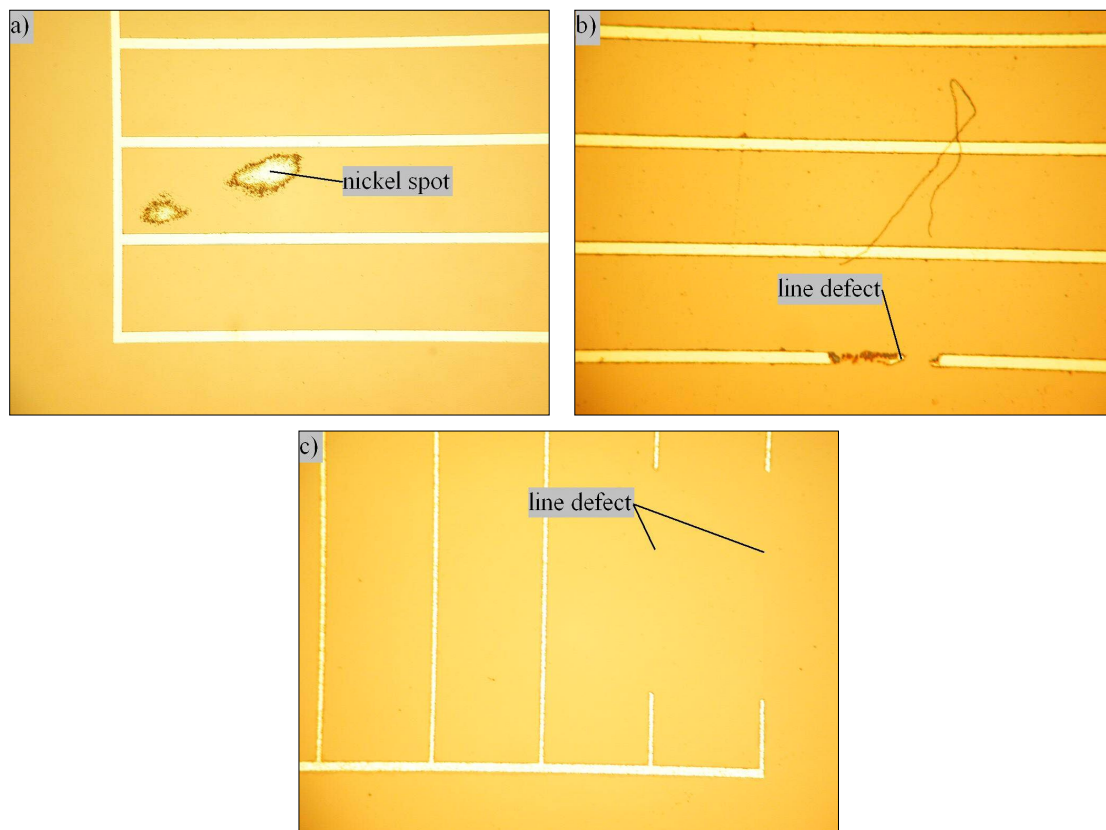


Figure A.1: Optical microscope pictures of a) nickel spot near the 25 μm anode (MEA 1), b) line break in the 25 μm anode (MEA 3) and c) two line breaks of the 10 μm anode (MEA 2).

The nickel spot in Figure A.1 a) seems to have resulted from a thick coating of photoresist. The thicker parts in a photoresist coating will not completely de-polymerize when exposed to UV radiation that has been calibrated for thinner

coatings. Therefore during the developing phase not all of the thick part of the photoresist will be washed away and so the nickel underneath this resist is protected from attacking acid in proceeding steps. A particle on the nickel surface during the spin phase of the lithography process may have caused build up of photoresist in this area. The build up photoresist was observed at the edges of all electrolytes during the resist spin phase. The resulting Ni left behind on the perimeter of the electrolytes looks similar to the Ni spot in Figure A.1 a) therefore this phenomena is believed to be responsible for the defect. However, this defect was not in electronic communication with the anode part and so it was assumed not to take part in the anode's electrochemistry.

The line break in figure A.1b) seems to be caused by a localized thin coating of photoresist. The discolored nickel left behind indicates that the photoresist in this area did not provide the nickel line with sufficient protection from the acid in the etching steps of lithography. The nickel line breaks in figure A.1 c) is caused by a different phenomenon because there is no residual Ni on the YSZ where the strips are missing. It is believed that the Ni did not adhere well to the YSZ in this area during sputter depositions possible due to impurities on the YSZ surface. Therefore, it is likely that these sections of the lines broke off in the agitated acid bath.

The missing amount of nickel area and TPB was estimated from the pictures using the nearby line widths as a measurement scale. The uncertainty in the calculation of missing Ni and TPB was chosen to be half the width of the strip used as a scale. The

defect in the 25 μm anode from MEA 3 was estimated to cause a loss of $0.0050 \text{ mm}^2 \pm 0.0004 \text{ mm}^2$ or $0.55 \% \pm 0.05 \%$ of the expected nickel coverage area and a loss of $400 \mu\text{m} \pm 50 \mu\text{m}$ or $0.57 \% \pm 0.07 \%$ of the expected TPB. The line breaks from the 10 μm anode from MEA 2 was estimated to be $0.0110 \text{ mm}^2 \pm 0.0002 \text{ mm}^2$ or $2.50 \% \pm 0.04 \%$ of the expected nickel coverage area and a loss of $960 \mu\text{m} \pm 40 \mu\text{m}$ or $1.36 \% \pm 0.06 \%$ of the expected TPB. The Ni loss from these anodes was considered small and therefore its impact on the electrochemical results was neglected.

Bibliography

- (1) de Boer, B. SOFC Anode - Hydrogen oxidation at porous nickel and nickel/yttria-stabilized cermet electrodes. University of Twente, 1998.
- (2) Mizusaki, J.; Tagawa, H.; Saito, T.; Yamamura, T., Kinetic studies of the reaction at the nickel pattern electrode on YSZ in H₂-H₂O atmospheres. *Solid State Ionics* **1994**, 70/71, 52-58.
- (3) Bieberle, A. The Electrochemistry of Solid Oxide Fuel Cell Anodes: Experiments, Modeling, and Simulations. Swiss Federal Institute of Technology, Zurich, 2000.
- (4) Larminie, J.; Dicks, A., *Fuel Cell Systems Explained*. ed.; John Wiley & Sons, LTD: 2000.
- (5) Weller, M.; Khelfaoui, F.; Kilo, M.; Taylor, M. A.; Argirusis, C.; Borchardt, G., Defects and phase transitions in yttria- and scandia-doped zirconia. *Solid State Ionics* **2004**, 175, 329-333.
- (6) Srinivasan, S.; Dave, B. B.; Murugesamoorthi, K. A.; Parthasarathy, A.; Appleby, A. J., *Fuel Cell Systems*. ed.; Plenum Press: New York, 1993.
- (7) Ivers-Tiffée, E.; Virkar, A. V., *High Temperature Solid Oxide Fuel Cells Fundamentals, Design and Application*. ed.; Elsevier Advanced Technology: Oxford, UK, 2003.
- (8) Jiang, Y.; Virkar, A. V., A High Performance, Anode-Supported Solid Oxide Fuel Cell Operating on Direct Alcohol. *Journal of the Electrochemical Society* **2001**, 148, (7), A706-A709.
- (9) Kee, R. J.; Zhu, H.; Goodwin, D. G., Solid-Oxide Fuel Cells with Hydrocarbon Fuels.
- (10) Park, S.; Craciun, R.; Vohs, J. M.; Gorte, R. J., Direct Oxidation of Hydrocarbons in a Solid Oxide Fuel Cell I. Methane Oxidation. *Journal of the Electrochemical Society* **1999**, 146, (10), 3603-3605.
- (11) Weber, A.; Sauer, B.; Müller, A. C.; Herbstritt, D.; Ivers-Tiffée, E., Oxidation of H₂, CO, and methane in SOFCs with Ni/YSZ-cermet anodes. *Solid State Ionics* **2002**, (152-153), 543-550.
- (12) Liu, J. A.; Barnett, S. A., Operation of anode-supported solid oxide fuel cells on methane and natural gas. *Solid State Ionics* **2003**, 158, (11).

- (13) Mogensen, M.; Krammer, K., Conversion of Hydrocarbons in Solid Oxide Fuel Cells. *Annu. Rev. Mater. Res.* **2003**, 33, 321-331.
- (14) Sukeshini, A. M.; Habibzadeh, B.; Becker, B. P.; Pomfret, M. B.; Demircan, O.; Walker, R. A.; Eichhorn, B. W.; Jackson, G. S., Electrochemical Oxidation of H₂, CO and H₂/CO Mixtures on Patterned Ni Anodes on YSZ Electrolytes. *Journal of the Electrochemical Society* **2005**.
- (15) McIntosh, S.; He, H. P.; Lee, S. I.; Costa-Nunes, O.; Krishnan, V. V.; Vohs, J. M.; Gorte, R. J., An examination of carbonaceous deposits in direct-utilization SOFC anodes. *Journal of the Electrochemical Society* **2004**, 151, (4), A604-A608.
- (16) Zhu, W. Z.; Deevi, S. C., A review on the status of anode materials for solid oxide fuel cells. *Materials Science and Engineering* **2003**, A362, 228-239.
- (17) Horita, T.; Sakai, N.; Kawada, T.; Yokokawa, H.; Dokiya, M., Oxidation and Steam Reforming of CH₄ on Ni and Fe Anodes under Low Humidity Conditions in Solid Oxide Fuel Cells. *Journal of the Electrochemical Society* **1996**, 143, (4), 1161-1168.
- (18) Walters, K. M.; Dean, A. M.; Zhu, H.; Kee, R. J., Homogeneous kinetics and equilibrium predictions of coking propensity in the anode channels of direct oxidation solid-oxide fuel cells using dry natural gas. *Journal of Power Sources* **2003**, 123, 182-189.
- (19) Blomen, L. J. M. J.; Mugerwa, M. N., *Fuel Cell Systems*. ed.; Plenum Press: New York, 1993.
- (20) Poulsen, F. W., Defect chemistry modeling of oxygen-stoichiometry, vacancy concentrations, and conductivity of (La_{1-x}Sr_x)_yMnO_{3 ± δ}. *Solid State Ionics* **2000**, 129, 145-162.
- (21) Baker, R. T.; Metcalfe, I. S., Study of the Activity and Deactivation of Ni-YSZ Cermet in Dry CH₄ Using Temperature-Programmed Techniques. *Ind, Eng. Chem. Res.* **1995**, 34, 1558-1565.
- (22) Winkler, W., *High Temperature Solid Oxide Fuel Cells, Fundamentals, Design and Applications*. ed.; Elsevier Ltd: New York, 2003.
- (23) Bard, A. J.; Faulkner, L. R., *Electrochemical Methods Fundamentals and Applications*. second edition ed.; John Wiley & Sons, Inc.: New York, 2001.
- (24) Tsai, T.; Barnett, S. A., Sputter deposition of cermet fuel electrodes. *J. Vac. Sci. Technol.* **1995**, 13, (3), 1073-1077.

- (25) Bebelis, S.; Zeritis, A.; Tiropani, C.; Neophytides, S. G., Intrinsic Kinetics of the Internal Steam Reforming of CH₄ over a Ni-YSZ-Cermet Catalyst-Electrode. *Ind. Eng. Chem. Res.* **2000**, 39, 4920-4927.
- (26) Holtappels, P.; De Haart, L. G. J.; Stimming, U.; Vinke, I. C.; Mogenssen, M., Reaction of CO/CO₂ gas mixtures on Ni-YSZ cermet electrodes. *Journal of Applied Electrochemistry* **1999**, 29, 561-568.
- (27) Jiang, Y.; Virkar, A. V., Fuel Composition and Diluent Effect on Gas Transport and Performance of Anode-Supported SOFCs. *J. Electrochem. Soc.* **2003**, 150, (7), A942-A951.
- (28) Bieberle, A.; Meier, L. P.; J., G. L., The Electrochemistry of Ni Pattern Anodes Used as Solid Oxide Fuel Cell Model Electrodes. *Journal of the Electrochemical Society* **2001**, 148, A646-A656.
- (29) Hu, J. T.; Jantunen, H.; Uusimaki, A., *J. Euor. Cer. Soc.* **2004**, 24, 1111.
- (30) Sureshini, A. M.; Habibzadeh, B.; Becker, B. P.; Pomfret, M. B.; Demircan, O.; Walker, R. A.; Eichhorn, B. W.; Jackson, G. S. In *CO and CH₄ Electrochemical Oxidation On Ni Patterned Anodes*, SOFC IX, Quebec City, Canada, 2005; Quebec City, Canada, 2005.
- (31) Adler, S. B., Reference Electrode Placement in Thin Solid Electrolytes. *J. Electrochem. Soc.* **2002**, 149, (5), E166-E172.
- (32) Lauvstad, G. O.; Tunold, R.; Sunde, S., Electrochemical Oxidation of CO on Pt and Ni Point Electrodes in Contact with an Yttria-Stabilized Electrolyte. *J. Electrochem. Soc.* **2002**, 149, (12), E506-E514.
- (33) Pettinger, B., *Adsorption of Molecules at Metal Electrodes*. ed.; VCH Publishers, Inc.: New York, 1992.
- (34) Nakamoto, K., *Infrared and Raman Spectra of Inorganic and Coordination Compounds*. 5th ed.; John Wiley & Sons, Inc.: New York, 1997.
- (35) Wolf, S.; Tauber, R. N., *Silicon Processing for the VLSI Era*. ed.; Lattice Press: Sunset Beach, 1986; 'Vol.' 1 - Process Technology.
- (36) Aaberg, R. J.; Tunold, R.; Mogenssen, M.; Berg, R. W.; Odegard, R., Morphological Changes at the Interface of the Nickel-Yttria Stabilized Zirconia Point Electrode. *J. Electrochem. Soc.* **1998**, 145, (7), 2244-2252.
- (37) Gubner, A.; Landes, H.; Metzger, J.; Seeg, H.; Struber, R. In *Solid Oxide Fuel Cells V*, The Electrochemical Society Proceedings Series, Pennington, NJ, 1997; Dokiya, M.; Yamamoto, O.; Tagawa, H.; Singhal, S. C. Pennington, NJ, 1997.

- (38) Waldbillig, D.; Wood, A.; Ivey, D. G., Thermal analysis of the cyclic reduction and oxidation behavior of SOFC anodes. *Solid State Ionics* **2005**, 176, 847-859.
- (39) Fisher, C. A. J.; Matsubara, H., Molecular dynamics simulations of interfaces between NiO and cubic ZrO₂. *Philosophical Magazine* **2005**, 85, (10), 1067-1088.
- (40) Vernoux, P.; Guindet, J.; Kleitz, M., Gradual Internal Methane Reforming in Intermediate-Temperature Solid-Oxide Fuel Cells. *J. Electrochem. Soc.* **1998**, 145, (10), 3487-3492.